Titre: Title:	Development of an Innovative Solution Minimizing RF Field Inhomogeneity and Energy Deposition in Ultra-High Field MRI Applications
Auteur: Author:	Gaspard Cereza
Date:	2022
Type:	Mémoire ou thèse / Dissertation or Thesis
Référence: Citation:	Cereza, G. (2022). Development of an Innovative Solution Minimizing RF Field Inhomogeneity and Energy Deposition in Ultra-High Field MRI Applications [Master's thesis, Polytechnique Montréal]. PolyPublie. https://publications.polymtl.ca/10282/

POLYTECHNIQUE MONTRÉAL

affiliée à l'Université de Montréal

Development of an innovative solution minimizing RF field inhomogeneity and energy deposition in ultra-high field MRI applications

GASPARD CEREZA

Institut de génie biomédical

Mémoire présenté en vue de l'obtention du diplôme de *Maîtrise ès sciences appliquées*

Génie biomédical

Avril 2022

POLYTECHNIQUE MONTRÉAL

affiliée à l'Université de Montréal

Ce mémoire intitulé :

Development of an innovative solution minimizing RF field inhomogeneity and energy deposition in ultra-high field MRI applications

présenté par **Gaspard CEREZA**

en vue de l'obtention du diplôme de *Maîtrise ès sciences appliquées*

a été dûment accepté par le jury d'examen constitué de :

Mohammad S. SHARAWI, président
Julien COHEN-ADAD, membre et directeur de recherche
Eva ALONSO ORTIZ, membre et codirectrice de recherche
David RUDKO, membre externe

ACKNOWLEDGEMENTS

I would first like to thank my supervisor Julien Cohen-Adad for the trust he put in me since my first steps within NeuroPoly, for always keeping a perfect balance between guidance and autonomy, and for his unfailingly precious and enlightening advice. Moreover, I would like to thank him for offering me the opportunity to explore the behinds of scientific research and to share what I learned with other students.

I would also like to thank Eva Alonso-Ortiz, Kyle Gilbert, Daniel Papp, and Nibardo Lopez-Rios for their invaluable help and their constant will to share their extensive knowledge.

Finally, I want to warmly thank Alexandre D'Astous for his friendliness and his brainpower that made our many collaborations always so pleasant and productive.

RÉSUMÉ

Bien qu'apportant de nombreux bénéfices en termes de qualité d'image, l'IRM à très hauts champ est particulièrement sensible aux artefacts liés à la réduction de la longueur d'onde du champ B_1^+ nécessaire pour basculer les spins hors de leur position d'équilibre. Cette longueur d'onde devenant plus petite que la plupart des régions du corps imagées, cela induit une inhomogénéité spatiale de l'angle de bascule qui, à son tour, entraine des variations d'intensité dans l'image finale. Afin de réduire ces inhomogénéités, des antennes équipées de plusieurs transmetteurs pouvant être excités en parallèle deviennent de plus en plus populaires pour l'imagerie à très haut champ, car la possibilité d'envoyer différentes impulsions à chaque transmetteur offre un meilleur contrôle sur les interférences radiofréquences. Ce procédé d'homogénéisation de champs est appelé B_1^+ shimming (ou RF shimming) et requière du matériel et des logiciels sophistiqués, ainsi que temps de scan supplémentaire, ce qui peut ralentir son intégration dans le milieu clinique.

Dans des régions telles que la moelle épinière, où les tissus présentent d'importantes variations en termes de propriétés électromagnétiques, cela devient encore plus difficile d'obtenir un champ B_1^+ homogène. La profondeur de la moelle épinière à l'intérieur du corps peut elle aussi limiter la puissance du champ B_1^+, résultant en un faible signal RM dans cette région. De plus, l'importante variabilité anatomique de la région vertébrale d'un patient à un autre vient elle aussi complexifier la création d'une impulsion qui résulterait en un angle de bascule spatialement homogène pour différents sujets.

L'objet de cette maîtrise consistait à développer un logiciel en libre-accès dédié au B_1^+ shimming, couvrant les scenarios les plus couramment utilisés et prenant en compte la déposition d'énergie dans les tissus afin d'assurer la sécurité du patient. La comptabilité avec des outils de segmentation automatique du cerveau et de la moelle épinière a également était implémentée afin de pouvoir effectuer un B_1^+ shimming ciblant ces régions spécifiques. Cette implémentation a été intégrée au projet *Shimming-Toolbox,* initialement développé homogénéiser le champ B_0.

Un test in-vivo a par la suite été effectué dans la moelle épinière à 7T et a montré une amélioration de l'homogénéité le long de la moelle épinière après B_1^+ shimming sur des images anatomique GRE et MP2RAGE, ainsi qu'une augmentation du signal dans la région thoracique.

ABSTRACT

While it offers important image quality benefits, Ultra-High Field MRI is particularly sensitive to RF related artifacts caused by the decreasing wavelength of the B_1^+ field required to flip the spins. This wavelength being smaller than most imaged body regions, it results in an inhomogeneous flip angle that induces intensity variations and local loss of signal across the image field of view. To reduce these inhomogeneities, multi-transmit coils with parallel transmission capability are becoming increasingly popular in UHF imaging, as they allow one to send different excitation pulses to each Tx element, providing better control of the RF interference pattern. This homogenization process is called B_1^+ shimming (or RF shimming) and requires complex hardware and software tools that hamper its clinical use.

In regions such as the spinal cord, where surrounding tissues present important variations in terms of electromagnetic properties, it gets even harder to obtain a homogeneous B_1^+ field. The depth of the spinal cord in the body may also hamper the generation of a sufficiently strong B_1^+ field in that region, resulting in a low MR signal. Moreover, the important anatomical variability of the spine region across patients further complicates the design of an excitation pulse that would result in robust inter-subject flip angle homogeneity. For these reasons, it is expected that performing patient-specific B_1^+ shimming with a focus on the spinal cord could improve the image homogeneity.

The focus of my master's project was on the development of an open-source B_1^+ shimming software solution that covers the most basic shimming scenarios and accounts for energy deposition in tissues, so as to ensure patient safety. Compatibility with brain and spinal cord segmentation tools was also implemented so that localised B_1^+ shimming could be performed over specific regions. This B_1^+ shimming implementation was integrated within the *Shimming-Toolbox* project, initially developed to homogenize the main static magnetic field B_0.

It was then tested in-vivo to perform patient specific B_1^+ shimming during spinal-cord imaging at 7T and resulted in an improved homogeneity in the spinal-cord on structural GRE and MP2RAGE images, with coefficients of variation reduced by up to 40% and 11% respectively, as well as in a recovered signal in the thoracic spinal cord.

TABLE OF CONTENTS

LIST OF TABLES

LIST OF FIGURES

LIST OF SYMBOLS AND ABBREVIATIONS

B_0	Main static magnetic field
B_1	Radiofrequency electromagnetic field
B_1^+	Transmit radiofrequency magnetic field
B_1^-	Receive radiofrequency magnetic field
CP	Circular polarization
DICOM	Digital imaging and communications in medicine
FA	Flip angle
GUI	Graphical user interface
IEC	International Electrotechnical Commission
MRI	Magnetic resonance imaging
NIfTI	Neuroimaging Informatics Technology Initiative
NMR	Nuclear magnetic resonance
pTx	Parallel transmission
RF	Radio frequency
Rx	Receive
ROI	Region of interest
SAR	Specific absorption rate
SNR	Signal to noise ratio
sTx	Single pulse transmission
T	Tesla
TR	Repetition time
Tx	Transmit
UHF	Ultra high field

VOP	Virtual observation point
γ	Gyromagnetic ratio
ω_0	Larmor frequency

CHAPTER 1 INTRODUCTION

In the late 20th century, Magnetic Resonance Imaging (MRI) emerged as a promising and minimally intrusive way to visualize the inside of the human body. MRI is based on the nuclear magnetic resonance (NMR) phenomenon first described and applied to individual isolated nuclei in 1938 by Isidor Isaac Rabi, who received a Nobel Prize in Physics for his work in 1944 [1]. The NMR phenomenon has then been independently demonstrated in condensed matter in 1946 by Felix Bloch [2] and Edward Mills Purcell [3], in water and paraffin respectively. They then jointly received the Nobel Prize in Physics in 1952. In 1971, Raymond Damadian proposed to use the NMR phenomenon for medical diagnosis. He had discovered that tumoral and healthy cells emitted distinguishable signals that could be isolated by an NMR scan [4]. Damadian and his team subsequently built the first whole-body MR scanner in 1977 [5]. In the meantime, Paul Lauterbur had shown in 1973 that NMR could be used to produce images and Peter Mansfield significantly improved the imaging process, turning the NMR phenomenon into a fast and promising imaging technique [6], [7]. Lauterbur and Mansfield were also jointly awarded the Nobel Prize in Medicine in 2003 for their contributions to what since became one of the most widely used biomedical imaging techniques.

Nowadays, part of the MRI research is caught in what resembles a “race towards the strongest magnetic field”. Indeed, since Peter Mansfield and his team acquired the first MR image of a human body part in 1977 (a finger’s cross section at 0.35T in 23 minutes), the static magnetic fields used in MRI have never ceased to increase. While most present-day clinical applications are performed on 1.5T and 3T scanners, Ultra High Field (UHF) imaging is becoming increasingly popular among the research community. As of early 2022, about one hundred 7T scanners can be found around the world and some of them are starting to be used in clinical applications, the first 10.5T in-vivo brain images have been published a few years back [8], and the strongest whole-body scanner in the world, with a nominal field strength of 11.7T, recently successfully provided high resolution images of a pumpkin. The main motivations behind this race towards strong magnetic fields are the signal to noise ratio (SNR) and contrast gains associated with UHF imaging [9]–[12].

The benefits of UHF MRI come with many technical challenges, some of them related to the increased frequency of the RF fields required to produce the images. Indeed, the use of higher frequencies implies a reduction of the RF wavelength which may become smaller than the imaged

region, resulting in an inhomogeneous RF field strength across the image. These inhomogeneities are further increased when several transmit elements are used simultaneously, as the different RF waves will interact to produce constructive and destructive interferences [13], [14]. A way to mitigate this inhomogeneity is to monitor the magnitudes and phases of the excitation pulses sent on the different transmit (Tx) elements in order to control the RF interference patterns so that the resulting field becomes homogeneous. This process is usually referred to as RF shimming or B_1^+ shimming [15]–[17].

To date, no open-source tool for performing B_1^+ shimming in a few minutes using in-vivo data collected directly at the scanner has been made available. An important part of this thesis was therefore dedicated to the development of such a tool and its integration within the *Shimming Toolbox* project (NeuroPoly, Montreal, Canada), initially created to perform B_0 shimming (homogenization of the main static magnetic field B_0) [18]. The main goal of this B_1^+ shimming implementation was to allow a user to perform a fast B_1^+ shimming experiment at the scanner by quickly measuring the RF field and running a few lines of code offline (not directly on the scanner console) with the possibility to target a specific body region to homogenize.

While different custom spine coils with parallel transmit (pTx) capabilities (i.e., the possibility to send different pulses to each Tx element) have been developed around the world [9], [19]–[24], no study assessing the benefits of B_1^+ shimming in the spinal cord has been conducted to our knowledge. For this reason, it was decided to test the newly implemented *Shimming Toolbox* B_1^+ shimming feature during in-vivo spinal cord imaging applications at UHF.

The second chapter of this thesis briefly introduces the different electromagnetic fields involved in acquisition of MR images, with a focus on the transmit radiofrequency field B_1^+ that provides an overview of the rationale behind B_1^+ shimming. This introduction comes along a critical literature review covering from the early days of B_1^+ shimming to state-of-the-art applications. The third chapter covers the implementation of a full B_1^+ shimming pipeline as a *Shimming Toolbox* feature, while the fourth chapter presents its application to spinal cord imaging at 7T. This will be followed by a fifth chapter dedicated to a discussion and a critical analysis of the results obtained. Finally, a conclusion chapter will wrap up this work and introduce future investigations that could be a relevant continuity to this work.

CHAPTER 2 LITERATURE REVIEW

2.1 Introduction to the different magnetic fields used in MRI

During an MRI scan, the patient is placed within three main types of magnetic fields generated by different sets of coils. Each one of these fields serves a very specific role in the image acquisition process, but they need to be jointly used with rigorous timing to obtain a faithful representation of the subject's tissues.

2.1.1 The main static field B_0

The main static magnetic field (B_0) is the strongest field involved in MRI experiments and is the main characteristic used to describe a scanner. Scanners are usually considered to operate in the UHF range when B_0 is greater or equal to 7T. B_0 is generated by a large superconductive magnet surrounding the patient and ideally remains constant over space and time. The role of B_0 is to align specific types of nuclei (spins) that present a dipole moment, giving rise to a net macroscopic magnetization at room temperature. In their equilibrium position along B_0, these spins follow the rules of quantum mechanics and precess (rotate) around the B_0 axis at a specific frequency (Larmor frequency), given by:

$$\omega_0 = \gamma B_0 \tag{2.1}$$

where ω_0 (in Hz) is the Larmor frequency, B_0 (in T) is the strength of the main static magnetic field and γ (Hz/T) is the gyromagnetic ratio, which is specific to the nuclei that are imaged. Only a few types of nuclei can be used to image the human body, the most common one being the hydrogen due to its abundance in the body as a component of the water molecules. The hydrogen nucleus (a single proton) has a gyromagnetic ratio γ_H of 42.58 MHz/T. At 7T, this results in a precession of the ^{1}H nucleus at $\omega_{0_{1H}} \approx 298$ MHz, which is close to the lower bound of the Ultra High Frequency range, as illustrated in Table 2.1. This is the reason why ultra high field imaging corresponds to B_0 values greater than 7T.

Table 2.1 The different radiofrequency ranges

Name	**Very Low Frequency**	**Low Frequency**	**Medium Frequency**	**High Frequency**	**Very High Frequency**	**Ultra High Frequency**	**Super High Frequency**	**Extremely High Frequency**
Frequency range	**3kHz - 30kHz**	**30kHz - 300kHz**	**300kHz - 3MHz**	**3MHz - 30MHz**	**30MHz - 300MHz**	**300MHz - 3GHz**	**3GHz - 30GHz**	**30GHz - 300GHz**

As briefly explained above, the role of the B_0 field is to give rise to an equilibrium state where a net macroscopic magnetization, resulting from the contribution of all the individual moments of the spins present in the body, is oriented along the B_0 field. This longitudinal equilibrium magnetization M_0 is given by the following formula [25]:

$$M_0 = \frac{\rho \gamma^2 \hbar^2}{4kT} B_0 \qquad (2.2)$$

where ρ is the spin density (the number of protons per unit volume), $\hbar$ is the reduced Planck constant ($1.05e^{-34}$ joule.s), k is the Boltzmann constant and T is the temperature.

This equation shows that the equilibrium magnetization scales linearly with B_0, as well as with the spin density ρ. The magnetic resonance signal measured to reconstruct an MR image being directly proportional to M_0, this implies that, for a same spin density, UHF MRI yields a higher signal than low field applications. This increased signal can notably also be used to improve the image resolution (imaging smaller voxels containing less spins) while preserving the same signal strength as low field imaging. When trying to visualize very small tissues or to precisely localize functional activities, the high resolution associated with UHF imaging may thus highly improve the diagnostic benefits of the images [11]. Another possible use of this increased signal is to reduce the total scan time, for example by performing parallel imaging with higher acceleration factors without SNR reduction compared to lower field strength, which is of interest for clinical applications where some patients might have to spend up to an hour in the scanner [26], [27].

2.1.2 The magnetic gradients

To reconstruct an image of the inside of the body, one needs to know where the measured signal is originating from. To this end, 3 additional sets of coils are used to produce gradient magnetic fields in the x, y, and z directions. These gradients spatially modulate the z component of the B_0 field, therefore encoding the position of the spins in their local precession frequency $\omega_0(x, y, z)$. Performing a Fourier transform of the measured MR signal then allows us to separate its frequency components, and to associate each one of these frequencies with a specific point of the image. The intensity of a point of the image is then proportional to the spin density at this location, providing the contrast of the image.

The x, y and z gradients can be simultaneously monitored to encode the spatial information in any arbitrary direction, making the MR acquisition possible for any slice orientation. As the Fourier theory is not limited to 2D signals, this principle can be extended to 3D volumes and used to perform fast 3D MRI.

As the magnetic gradients theory lies a bit out of the scope of this work, it will not be further detailed here, but as an essential component of the MRI workflow, it was deemed relevant to briefly introduce it.

2.1.3 The B_1 field

The measured MR signal is obtained by exciting the spins out of their equilibrium position and measuring the signal they emit while returning to equilibrium along the z axis (the direction of B_0), during a process called relaxation. Two types of relaxation exist, one along the longitudinal z axis due to spin-lattice interactions [28] (associated to a relaxation time T_1) and one in the x-y transversal plane due to spin-spin interactions (associated to a relaxation time T_2) [2]. These two types of relaxation can be combined with the timing of MRI sequences to provide different contrasts between the tissues.

The tipping of the net magnetization out of its equilibrium state is performed by applying a transverse radiofrequency electromagnetic field (called B_1 or RF field) at the Larmor frequency. This B_1 field is composed of two circularly polarized complex components, referred to as $\widehat{B}_1^+$ and $\widehat{B}_1^-$ and defined as [29], [30]:

$$\hat{B}_1^+ = \frac{\left(\hat{B}_{1x} - i\hat{B}_{1y}\right)}{\sqrt{2}} \tag{2.3}$$

$$\hat{B}_1^- = \frac{\left(\hat{B}_{1x} + i\hat{B}_{1y}\right)}{\sqrt{2}} \tag{2.4}$$

where $\hat{B}_{1x}$ and $\hat{B}_{1y}$ are the x and y components of the B_1 field. For simplicity, $\hat{B}_1^+$ and $\hat{B}_1^-$ will sometimes be written B_1^+ and B_1^- in the rest of this work.

On resonance, only the B_1^+ component is efficient in flipping the spins, because it precesses in the same direction as the Larmor precession, while B_1^- precesses in the opposite direction and will be related to the signal reemitted by the spins after excitation that will induce a current in the receive RF elements.

The amplitude of the measured MR signal is proportional to the equilibrium magnetization M_0 which is itself proportional to B_0, as discussed previously. But the MR signal amplitude also depends on the flip angle (FA), which is the angle by which the magnetic moment has been deflected from its equilibrium position. The FA relates to the B_1^+ field according to

$$\theta = \gamma \int_0^\tau |B_1^+(t)| dt \tag{2.5}$$

where θ is the FA, $|B_1^+(t)|$ is the amplitude of the B_1^+ field at time t, and τ is the duration of the excitation pulse.

Equation (2.5) shows that a stronger or longer B_1^+ pulse will result in a larger flip angle. The receive coils (Rx elements), that measure the MR signal used to reconstruct the image, are positioned in such a way that the maximum signal is obtained for a FA of 90°, i.e., when the net magnetization is fully tilted in the transversal plane. Assuming a rectangular excitation pulse ($\theta = \gamma\tau|B_1^+|$), the relation between the B_1 field and the image intensity (I) can we written as [31]

$$I \propto \rho \, sin\left(\gamma\tau|\hat{B}_1^+|\right)\left|(\hat{B}_1^-)^*\right| \tag{2.6}$$

The local image intensity therefore directly depends on the local strength of the B_1 field.

2.2 RF inhomogeneities

The dependency of the image intensity on the B_1 field strength has a straightforward consequence: if the flip angle varies across the image field of view, similar tissues with the same spin density and relaxation constants may appear with different image intensities, depending on their spatial location.

2.2.1 B_1^+ inhomogeneities at UHF

The B_1^+ field is produced by the transmit (Tx) system of the scanner. For low-field application, the transmit coils can be placed in the scanner bore, far from the patient body. At UHF however, several Tx elements placed close to the patient are generally used to reduce undesired standing wave effects and to limit the energy deposition in the tissues that could cause them to heat up. These effects mostly result from the high frequency of the B_1^+ field required to tilt the net magnetization M_0 in the transverse plane. Indeed, equation (2.1) states that the Larmor Frequency is linearly proportional to the B_0 strength. As the B_1^+field needs to oscillate at the Larmor frequency to efficiently flip M_0, this therefore results in a decreased $\lambda_{B_1^+}$ wavelength at UHF according to

$$\lambda_{B_1^+} \propto \frac{1}{\sqrt{\epsilon_r} B_0} \tag{2.7}$$

where ϵ_r is the relative permittivity of the medium, which varies across human tissues but remains in the same order of magnitude as the permittivity of water ($\epsilon_{water} \approx 80$) in the UHF range without ever exceeding it [32], [33]. At 7T, the RF wavelength in water for ^{1}H imaging is about 11cm [34], which is smaller than most imaged body regions.

Due to this reduced wavelength, the phase of the B_1^+ field produced by a single Tx element varies across the image field of view, and when several elements are used simultaneously, RF interferences occur, giving rise to hotspots (constructive interferences) or extinctions (destructive interferences) in certain regions of the image.

As mentioned above, the small wavelength also causes undesired dielectric effects (interactions between the tissues and the electrical component of the B_1^+ field), such as the standing wave effect that may arise when RF waves are refracted at tissue interfaces [13]. Central brightening on brain

images, which is notably observed at 3T [14], is a direct consequence of the standing wave effect. The electric component of the B_1^+ field is also responsible for the heating of the tissues due to resistive (induced ionic currents) and dielectric (vibration of the water molecules) thermal effects that are one of the major safety concerns about UHF MRI and will be more thoroughly discussed later.

The absorption of RF waves by human tissues increases with the their frequency [35]. In UHF MRI, this may result in lower B_1^+ values at depth compared to lower field strength, further increasing the heterogeneity of the B_1^+ field across the images field of view.

2.2.2 Receive coil sensitivity

The linear dependency of the image intensity on $\left|\hat{B}_1^-\right|^*$, illustrated by equation (2.6), states that the image intensity is also affected by the inhomogeneity of the MR signal reemitted by the spins during relaxation. Moreover, the reception profiles (sensitivity) of the receive coil is not spatially homogenous, further affecting the image intensity [36]. Indeed, depending on their geometry, the receive (Rx) elements placed all around the imaged region do not exhibit a spatially constant sensitivity to the B_1^- field. The low sensitivity regions of the image will thus appear darker than the high sensitivity regions, even if the imaged tissue is the same. This implies that even with a perfectly homogeneous B_1^+ field, sensitivity inhomogeneities will still affect the image intensity.

2.3 Correcting the B_1^+ inhomogeneities

As mentioned in the previous section, inhomogeneous B_1^+ fields affects the intensity and contrast of the MR images and may hamper their use for an accurate diagnostic application [37]. Motivated by the potential benefits of UHF imaging in terms of image SNR, CNR, resolution and imaging speed, various solutions have been proposed over the last two decades in order to mitigate the influence of the B_1^+ inhomogeneities on the MR images. This process is usually referred to as B_1^+ shimming (or RF shimming) [15]–[17].

2.3.1 Coil design

When seeking to produce a homogeneous B_1^+ field, one of the first things to work on is the design of the coil. The positioning of the Tx and Rx elements, their geometry, their decoupling, or the materials used for the different parts of the coils are notable parameters that can greatly affect the B_1^+ distribution and the B_1^- sensitivity. For this reason, various types of coils have been proposed in the literature [23], [38]–[40] and several iterations are often necessary to obtain a satisfyingly optimized coil design suited to one's imaging needs [41]. While a strategic coil design might reduce the influence of the RF inhomogeneities, it is usually not sufficient to completely compensate for them at UHF. Moreover, the B_1 distribution is also greatly affected by the anatomical variations across subjects, making it highly challenging to find an ideal coil design that produces a homogeneous B_1 field for all subjects. Coil design strategies thus need to be associated with additional B_1^+ shimming methods to obtain homogeneous images.

2.3.2 Passive B_1^+ shimming

Positioning high permittivity materials (e.g., pads filled with highly conductive substances such as manganese chloride) close to the imaged region may reduce the RF inhomogeneities [42]–[45], notably by improving the impedance matching between the subject and the coil, resulting in a better RF propagation in the body. However, it remains very challenging to efficiently improve the image homogeneity with dielectric padding, as homogenizing the transmit field may simultaneously result in a heterogeneous receive sensitivity [43]. Using these "passive" shimming methods along with careful coil design is however an interesting way to improve the quality of MR images acquired at UHF without additional scan time.

2.3.3 Image processing

Another way to deal with RF inhomogeneities without lengthening the scan duration is to use post-processing techniques to evaluate the influence of the RF inhomogeneities on the image and to compensate for them [46]. Similar correction approaches based on a direct measurement of the B_1^+ and reception sensitivity maps have also been developed, providing a better estimation of the RF inhomogeneities at the cost of additional scan time dedicated to the mapping process [47].

While these post-processing methods efficiently mitigate the RF inhomogeneities on a patient-specific basis and do not require any additional hardware equipment, they however cannot improve the SNR and CNR of the original images, as the intensity corrections are applied once the images have already been acquired in the presence of RF inhomogeneities. Moreover, low signal regions cannot be accurately compensated by these methods.

2.3.4 Pulse design

To mitigate specific intensity inhomogeneity patterns, the shaping of the excitation waveform can be combined with precise timing of the gradient fields to obtain a particular B_1^+ distribution pattern that compensates for the image intensity variations. For example, fast-k_z pulses [48] are well suited to compensate for the central brightening observed on brain images acquired with volume coils at 3T, due to their gaussian shaped excitation pulses. Patient-specific pulse design techniques, such as the strongly modulating pulses that aim at optimally varying the phase of the RF pulse to rotate the net magnetization from the z-axis to a specified flip angle, based on preliminary measurements of the B_1 and B_0 distributions, have also been proposed in literature [49], [50], at the cost of additional scan time in order to acquire the necessary data and perform the pulse optimization process.

2.3.5 Circularly polarized excitation

UHF MRI coils are usually composed of several Tx elements. The simplest way to produce a B_1^+ field is to simultaneously send a single excitation pulse to all these Tx elements. However, due to the previously discussed sources of B_1^+ inhomogeneities at UHF, this pulse excitation is likely to result in an inhomogeneous image intensity. The total B_1^+ field produced by N_{Tx} transmit elements can be formulated as

$$B_1^+ = \sum_{n}^{N_{Tx}} {B_1^+}_n \tag{2.8}$$

where ${B_1^+}_n$ is the individual complex transmit field produced by the n^{th} transmit element.

For specific coil architectures, such as birdcage coils with N_{Tx} regularly spaced Tx elements (rungs), using hardware that induce a $\frac{2\pi}{N_{Tx}}$ phase shift between consecutive Tx elements (quadrature excitation) results in a circularly polarized B_1^+ field now expressed as

$$B_1^+ = \sum_{n}^{N_{Tx}} {B_1^+}_n e^{\frac{i2\pi n}{N_{Tx}}} \quad (2.9)$$

that more efficiently tilts the spins out of their equilibrium position [51]. This circular polarization (CP) mode reduces the required excitation power, increases the SNR, and may also improve the B_1^+ homogeneity by modifying the RF interference patterns in the imaged tissues.

For more complex coil designs, different phase shifts values providing similar benefits as the CP mode can be determined from electromagnetic simulations or experimental measurements and be used as a "pseudo" CP mode for the coil.

2.3.6 Parallel transmission

Most of the recent UHF MRI scanners feature a complex and expensive parallel transmission (pTx) system that offers the possibility to simultaneously send different excitation pulses to each Tx element [52]. Therefore, pTx systems might provide a high degree of freedom for controlling the RF interference patterns and for mitigating the B_1^+ inhomogeneities at UHF.

2.3.6.1 Static B_1^+ shimming

Since the pTx system allows one to send different pulses to each Tx element, it can be used in CP mode by digitally controlling the phase shifts between all the pulses. As a non-patient specific excitation that does not require any additional scan time, a coil's CP mode will usually be used as the default excitation mode on pTx systems. However, instead of simply setting the phases to the default CP mode values, it is also possible find a patient-specific set of phases that will further homogenize the B_1^+ distribution in the region of interest, as long as a previous measurement of the B_1^+ field (B_1^+ mapping) has been performed [15]. The process of using phase values optimized from in-vivo measurement of the B_1^+ field is referred to as phase-only shimming.

An even more efficient, but also more computationally demanding, method is the optimization of both the magnitude and phase values applied to the different Tx elements. This process is usually referred to as static B_1^+ shimming, or sometimes simply as B_1^+ shimming. Here, the optimization process aims at finding a set w of N_{Tx} complex values, called shim weights, that correspond to the magnitude and phase values of the excitation waveforms applied on the Tx elements to produce a total B_1^+ field expressed as

$$B_1^+ = \sum_n^{N_{Tx}} \boldsymbol{w_n} B_{1\,n}^+ = \sum_n^{N_{Tx}} \boldsymbol{A_n} B_{1\,n}^+ e^{i\boldsymbol{\phi_n}} \qquad (2.10)$$

where $w_n = A_n e^{\phi_n}$ is the complex shim weight applied on the n^{th} Tx element.

Depending on the chosen optimization parameters, the optimized shim weights may not only result in a homogenized B_1^+ field, but also reduce the energy deposition in the tissues [53] or provide a high B_1^+ efficiency [54]. It has been shown that static B_1^+ shimming is more efficient over a small ROI and with a large number of shim elements, due to the increased number of degrees of freedom available for the optimization process [55]. However, this method is unlikely to result in a perfectly homogeneous B_1^+ distribution, as the number of degrees of freedom always remains limited, and hardware and safety constraints may hamper the optimization efficiency. Indeed, the shim weights values are notably limited by hardware limitations on the maximum power that can be sent by the Tx amplifier to the Tx coil, and by Specific Absorption Rate limitation guidelines that will be discussed later. As a result, the maximum B_1^+ efficiency that can be reached is limited, and optimal homogeneity will more easily be obtained with low shim weights magnitude values that are less likely to exceed these limitations.

Performing static B_1^+ shimming usually takes between 5 and 15 minutes of additional scan time per patient, as it requires a mapping step and a shim weights optimization process.

2.3.6.2 Transmit-SENSE

Combining parallel transmission and a RF pulse optimization that accounts for the spatial sensitivity of each Tx elements results in what is usually referred to as transmit-SENSE (transmit sensitivity encoding) [56]. Adding a temporal dependence to the excitation pulses further increases the optimization freedom, allowing for a more homogeneous B_1^+ field.

$$B_1^+ = \sum_n^{N_{Tx}} \boldsymbol{A_n(t)} {B_1^+}_n e^{i\boldsymbol{\phi_n(t)}} \quad (2.11)$$

In addition to improving the RF homogeneity, strategic pulse design associated with pTx can also reduce the amount of energy deposited in the patient's tissue and shorten the repetition time (TR) of the imaging sequences [57].

To date and to my knowledge, transmit-SENSE is the most efficient way of homogenizing the B_1^+ field, but it is also the most complex to perform as it requires additional scan time, sophisticated hardware equipment and computationally demanding pulse optimization algorithms.

2.3.7 Calibration-free methods

Many of the previously discussed methods require additional scan time to efficiently homogenize the B_1^+ distribution. However, scan duration is a major concern regarding the integration of medical imaging modalities within clinics, and the need for additional scan time to reduce the RF inhomogeneities at UHF may hamper their path towards clinical routine.

To get rid of any additional scan time, recent works focused on the use of "plug-and-play" solutions that provide a homogeneous B_1^+ field without any calibration step, such as the Universal Pulses [58]. The idea here is to use calibration-free pulses that are optimized over a set of subjects rather than a single subject. As Universal Pulses are not patient-specific, they cannot homogenize the B_1^+ field as efficiently as transmit-SENSE methods, but they have been shown to outweigh static B_1^+ shimming for brain imaging applications [58], offering a promising trade-off between scan time and B_1^+ homogeneity. Calibration-free B_1^+ shimming can even be further improved by machine learning methods, as it was demonstrated by the SmartPulse technique [59]. However, these "plug-and-play" methods offer limited control over most acquisition parameters, as they are optimized for very specific imaging scenarios.

2.4 Challenges of static B_1^+ shimming

All the B_1^+ shimming methods presented above face specific obstacles and limitations that can be roughly simplified as a trade-off between shimming efficiency, scan-time, patient safety and

technical complexity. In this work, it was decided to implement a static B_1^+ shimming solution, as it can easily be used with many different sequences on pTx systems, while more efficient pulse optimization methods would have required to program specific imaging sequences, restricting them to a few types of sequences and scanners.

2.4.1 Hardware and software requirements

Performing static B_1^+ shimming requires complex hardware features such as multi-transmit coil arrays and parallel transmit (pTx) capability that allows one to send different excitation waveform to each Tx element, providing control on the B_1^+ interferences pattern. It also requires specific software solutions that can compute optimized shim weights from B_1^+ maps acquired at the scanner. As a state-of-the-art MRI feature, B_1^+ shimming is mainly performed by research teams around the world that develop internal code suited to their needs. And while many B_1^+ shimming scientific papers were accompanied by data and code, no open-source tool covering a complete static B_1^+ shimming experiment, from exporting the B_1^+ maps to inputting the optimized shim weights on the scanner, was found to be available.

2.4.2 Scan time

Due to the extensive investment the purchase, installation and maintenance of UHF MRI scanners represent, their number is restrained, and their availability is therefore particularly limited. Time is thus of the essence during a clinical MRI scan in order to scan as many patients as possible by limiting the duration of one's journey within the narrow scanner bore. Compared to a classic scan with no shimming, we saw that performing patient-specific static B_1^+ shimming requires additional scan time, mainly dedicated to mapping of B_1^+ field and optimizing the shim weights. Moreover, the subject's motion between the B_1^+ mapping process and the acquisition of the B_1^+ shimmed images may affect the shimming efficiency, and a fast scan reduces the odds of an important motion. In an effort to make static B_1^+ shimming a viable solution for future clinical use, it is thus primordial to come up with a solution that limits the additional scan time that it requires.

2.4.3 Energy deposition and patient safety

While MRI uses non-ionizing electromagnetic B_1 frequencies to tilt the net magnetization, this RF field still deposits some energy within biological tissues, due to their thermal interaction with the electrical component of B_1. This might result in a heating of the tissues that could kill the cells if the temperature rise becomes too high [60], [61].

When performing static B_1^+ shimming, the RF interference pattern is modified, changing the electrical B_1^+ component. This might result in local "hotspots" that could induce an overheating of the tissues. For that reason, energy deposition must be accounted for when performing B_1^+ shimming, to ensure patient safety. While methods to measure the local temperature of the tissues have been proposed in literature [62]–[65], they remain particularly challenging and have not yet made their way to routine use in either clinical imaging or research applications, making it impossible to monitor tissue heating in real-time. For that reason, B_1^+ shimming is often performed while applying a constraint on the maximum SAR (Specific Absorption Rate) during the optimization routine [53], [66], instead of directly limiting the temperature rise.

SAR is a metric used to quantify the energy deposition in biological tissue and corresponds to the rate of absorption of the RF power by the patient's tissues. It is thus expressed in units of W/kg. At a specific location and for a given type of tissue, SAR is expressed as

$$SAR = \frac{\sigma}{2\rho}|E|^2 \qquad (2.12)$$

where σ and ρ are the conductivity and density of the tissue, and E is the electric field produced by the RF coils at the tissue's location [67].

According to Faraday's law of induction, E scales with the frequency of the RF pulse (electromagnetic induction is larger at high frequencies). This implies that SAR increases quadratically with the frequency and therefore must be firmly monitored at UHF to ensure patient's safety.

The total amount of energy absorbed by the body is referred to as the whole-body SAR (SAR_{WB}), but as the human tissues and the B_1 field are not uniform, the energy deposition varies locally, SAR_{WB} therefore does not reflect the local heating of the tissues. For this reason, local SAR values

averaged over a specific mass of tissue are used to estimate the deposited energy more accurately. Since the temperature rise takes time to occur, SAR is averaged over long time periods covering several RF pulses. For this reason, the International Electrotechnical Commission (IEC) guidelines fix two averaging times of 10 s and 6 min. At 7T, IEC fixes the following limits: 6-min SAR_{10g} cannot exceed 10 W/kg in Normal mode and 20 W/kg in First-level mode and 10-s SAR_{10g} cannot exceed twice the 6-min limits [68].

However, just as temperature, SAR is hardly directly measurable during in-vivo experiments, mainly because locally measuring the electrical component of B_1^+ is particularly challenging [69]. Local SAR values are thus estimated based on electromagnetic simulations using realistic modelling of the RF coil and human body ensemble [70]. What makes local SAR particularly interesting for estimating the energy deposition during B_1^+ shimming experiments is the fact that it can be computed from a set of complex shim weight values w using Q-matrices as follows [71]:

$$SAR(r) = w^H Q(r) w \tag{2.13}$$

where ^{H} is the conjugate transpose operator and Q(r) is the Q matrix associated with the local volume of tissue r.

At 7T, each 1g and 10g volume of tissue thus has a corresponding Q-matrix obtained via the aforementioned simulation process, and safety factors are introduced to account for the differences between the modelling and the actual RF coil and human body ensemble. However, the simulation often yields a very large number of matrices to be used as a SAR constraint, making the optimization computationally demanding over large body regions. To overcome this obstacle, compression algorithms such as the virtual observation points (VOP) method have been proposed to reduce the number of matrices used to estimate the local SAR values by gathering the Q-matrices into subgroups based on their similarities [72], [73].

CHAPTER 3 B_1^+ SHIMMING SOFTWARE IMPLEMENTATION

The main axis of this project was the implementation of an open-access toolbox that covers the most classic B_1^+ shimming scenarios encountered in literature, providing an easy-to-use solution that could benefit research groups with limited expertise in this field.

As previously discussed, due to the limited number and extensive cost of MRI facilities, aiming for a short scan-time is particularly important during both clinical and research MRI applications. Moreover, long scans may also further affect the efficiency of the B_1^+ shimming due to patient motion. The duration of the complete shimming process was thus one of the major concerns to bear in mind during the implementation of this software.

Another important feature to implement was the compatibility of the code with automated segmentation tools that would allow the user to perform B_1^+ shimming over a specific region of interest (e.g., brain or spinal cord).

3.1 The *Shimming Toolbox* project

Initiated within NeuroPoly, the *Shimming-Toolbox* project [18] originally aimed at providing various B_0 shimming (homogenization of the main static field) methods. But as B_1^+ shimming applications are becoming increasingly popular, motivated by the fast development of UHF MRI technologies, it has been decided that B_1^+ shimming solutions should be part of the different features offered by *Shimming-Toolbox*. Initially developed in MATLAB (MathWorks, Natick, USA), *Shimming-Toolbox* has then been converted into Python, for the sake of open access and better compatibility with external tools such as automated segmentation pipelines, file conversion libraries or user interfaces. The *Shimming-Toolbox* code is openly available on GitHub, and anybody can contribute to its development.

3.2 B_1^+ mapping

Because every human being is anatomically unique, the B_1^+ distribution in the imaged volume changes from one subject to another due to a varying distribution of tissues with different electromagnetic properties. In order to homogenize the B_1^+ distribution in a specific region, patient-

specific shim weights optimization therefore requires prior knowledge of the B_1^+ field produced by each Tx element when the imaged subject is present within the scanner. These individual B_1^+ distributions can be measured via a process usually referred to as B_1^+ mapping, RF mapping, or flip-angle imaging [74]–[76].

For this work, access to a 7T Magnetom Terra scanner (*Siemens, Erlangen, Germany*) was provided. This scanner offers a product B_1^+ mapping sequence based on the pre-saturated TurboFLASH readouts method [77]. This sequence was deemed particularly interesting to use as a starting point for the *Shimming-Toolbox* B_1^+ shimming implementation, as it allows for a fast mapping of the B_1^+ phase and magnitude distributions produced by each Tx element over a selectable volume. Moreover, this sequence is expected to be available to most research groups working on 7T *Siemens* scanners, making them potential future users of the *Shimming-Toolbox* B_1^+ shimming features.

This B_1^+ mapping sequence assumes negligible T_1 relaxation between the pre-saturation and excitation pulses. This assumption benefits from the use of a centric reordering to favor the accuracy of the center of the k-space (low frequencies) by encoding it first after preparation (see [77] for more details about centric k-space reordering).

3.2.1 Converting the B_1^+ maps

Once the B_1^+ mapping has been performed, the measured B_1^+ phase and magnitude images are stored into multiple files that respect the Digital imaging and communications in medicine (DICOM) standards. Each DICOM file contains a 2D image along with metadata corresponding to the acquisition parameters. Storing the B_1^+ phase and magnitude produced by N_{Tx} elements over a volume containing N_{slices} slices therefore requires $2 \times N_{Tx} \times N_{slices}$ DICOM files. This rapidly results in hundreds to thousands of files for typical B_1^+ mapping (e.g., covering a brain volume with a 2mm isotropic resolution), inducing a risk to misplace some of them, and making the file management particularly cumbersome. To remedy this problem, it was decided to convert all the MRI volumes processed by *Shimming-Toolbox* to the Neuroimaging Informatics Technology Initiative (NIfTI) format that allows one to store several volumes into a single file. Moreover, NIfTI files can hold

complex values and are thus well suited for storing the B_1^+ maps that will be subsequently used for shimming.

The conversion from DICOM to NIfTI is performed using the *dcm2bids* Python converter, itself using the *dcm2niix* C++ conversion software. *dcm2bids* was chosen because it organizes the output files with respect to the Brain Imaging Data Structure (BIDS) convention which aims at standardizing the file organization of neuroimaging data, that are expected to represent a large portion of the data that will be processed by *Shimming-Toolbox*. After conversion, each NIfTI file is associated with a JSON file that carries metadata related to the MRI acquisition. Having this JSON file is useful because it can be opened in any text file reader to quickly identify the acquisition parameters, whereas NIfTI files necessitate specific applications to be able to visualize their content. A simplified representation of the whole conversion process is presented in Figure 3.1.

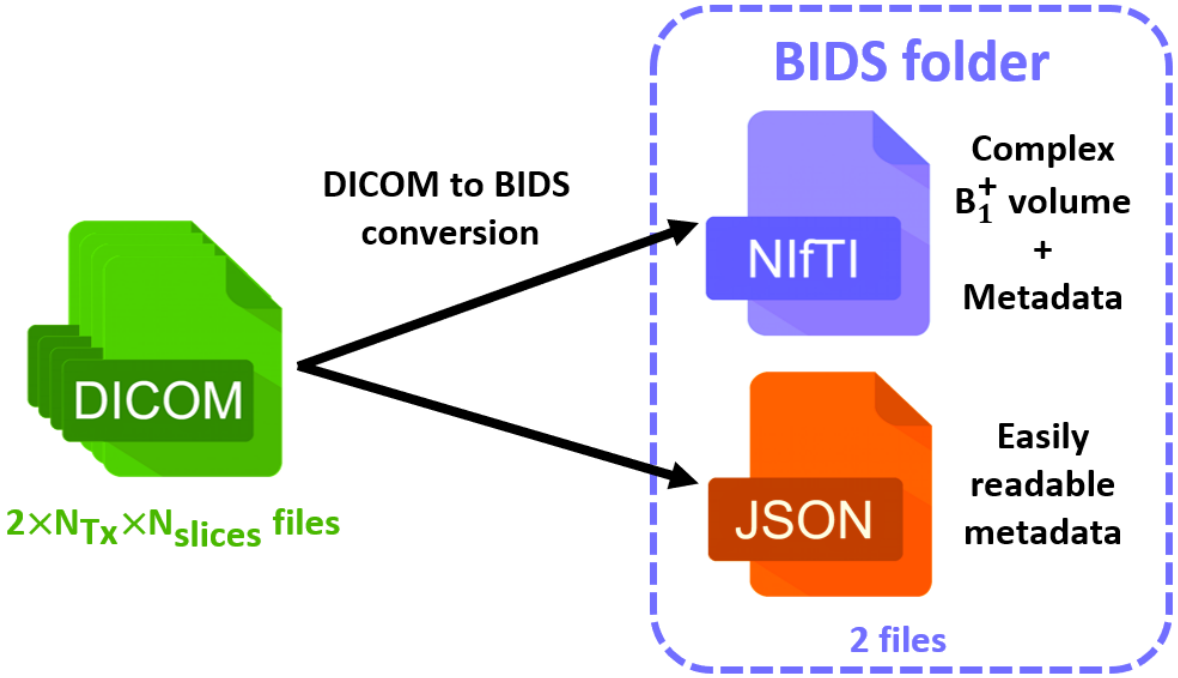

Figure 3.1 Schematic representation of the DICOM to BIDS conversion of the B_1^+ maps.

In *Shimming-Toolbox*, this conversion process is wrapped in a function that users can call via a command-line interface, by specifying the folder containing the DICOM files to convert and the

name of the imaged subject. This conversion step is always the first thing to perform when using *Shimming-Toolbox* with data acquired directly on the MRI scanner.

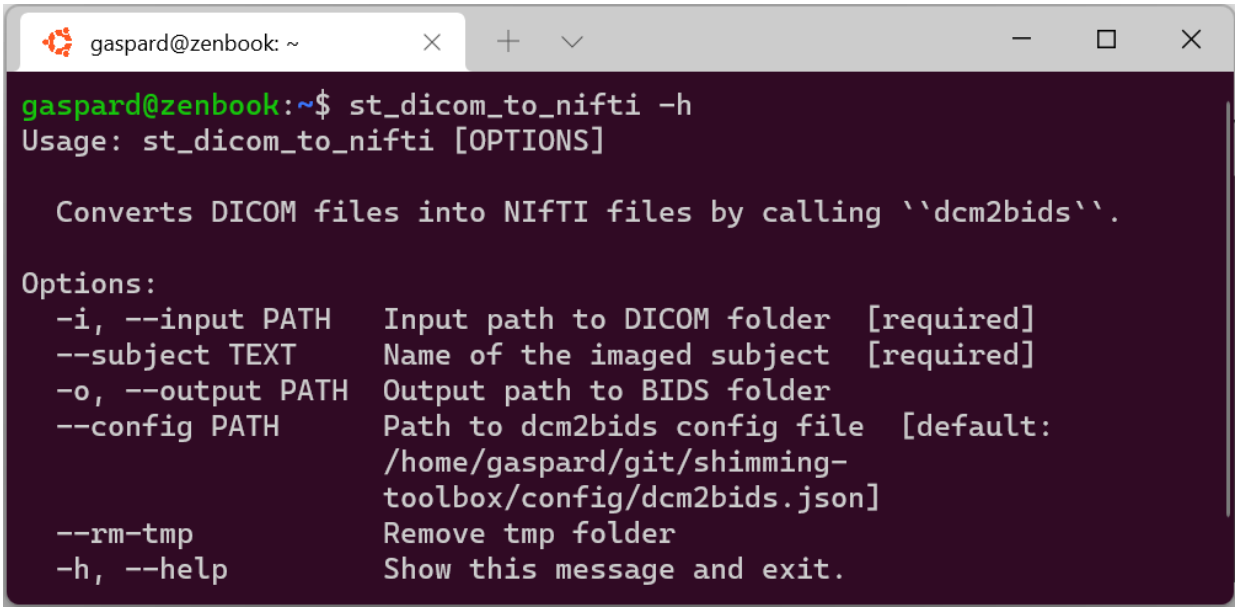

Figure 3.2 Contextual help of the "st_dicom_to_nifti" command line. Users can access it by typing "st_dicom_to_nifti -h" in their terminal.

Another benefit of handling NIfTI files with *Shimming-Toolbox* is their compatibility with numerous open-access tools such as the *Brain Extraction Tool* (BET) or the *Spinal Cord Toolbox* (SCT) that are open-source automated segmentation software.

3.2.2 Reordering and scaling the B_1^+ maps

Because of missing information in the DICOM headers provided by the TurboFLASH B_1^+ sequence, it is impossible for *dcm2niix* to identify which B_1^+ maps correspond to each Tx element. The different images are therefore shuffled in the converted NIfTI file. To remedy this, the pattern in which the images were shuffled was investigated and an "unshuffling" algorithm was implemented to reorganize the B_1^+ maps as 2 real matrices with dimensions $(x, y, N_{slices}, N_{Tx})$, corresponding to the phase and magnitude values of the B_1^+ field. The proposed unshuffling solution was tested over transversal, sagittal, coronal and arbitrarily oriented MRI volumes to assert its robustness with all types of B_1^+ maps acquired using the TurboFLASH B_1^+ mapping sequence on three different 7T scanners.

At this point, the unshuffled B_1^+ maps are stored as integer values ranging between 0 and 1800 for the magnitude (corresponding to 10 times the flip angle in degrees) and between 247 and 3847 for the phase. It was decided to rescale these values towards more intuitive units with physical meaning. It was chosen to express the magnitude values as the B_1^+ efficiency of the different transmit elements, which corresponds to the B_1^+ magnetic field produced for a fixed excitation voltage of 1 V. In literature, B_1^+ efficiency is usually expressed in nT/V. The rescaling of the magnitude values towards B_1^+ efficiency values was performed for each transmit element using the following formula (assuming a π-pulse of duration τ):

$$|B_1^+| = \frac{FA_{measured}}{10 \times FA_{saturation}} \times \frac{\pi}{\gamma \times \tau} \times \frac{1}{V_{ref}} \quad (3.1)$$

where $FA_{saturation}$=90° is hard-coded in the TurboFLASH B_1^+ mapping sequence and V_{ref} is the reference voltage applied during the mapping process.

The phase, on the other hand, is simply rescaled between -π and π as follows:

$$\angle B_1^+ = \frac{(\phi_{measured} - 2047) \times \pi}{1800} \quad (3.2)$$

Once rescaled, the magnitude and phase volumes are gathered into a single complex Python *numpy.ndarray()* object with dimensions (x, y, N_{slices}, N_{Tx}). Figure 3.3 shows in-vivo rescaled B_1^+ magnitude and phase distributions produced in a brain by a coil array with 8 Tx elements regularly positioned all around the patient. Here, a single slice in the center of the brain is shown for clarity, but a full brain volume has been acquired and stored in a NIfTI file.

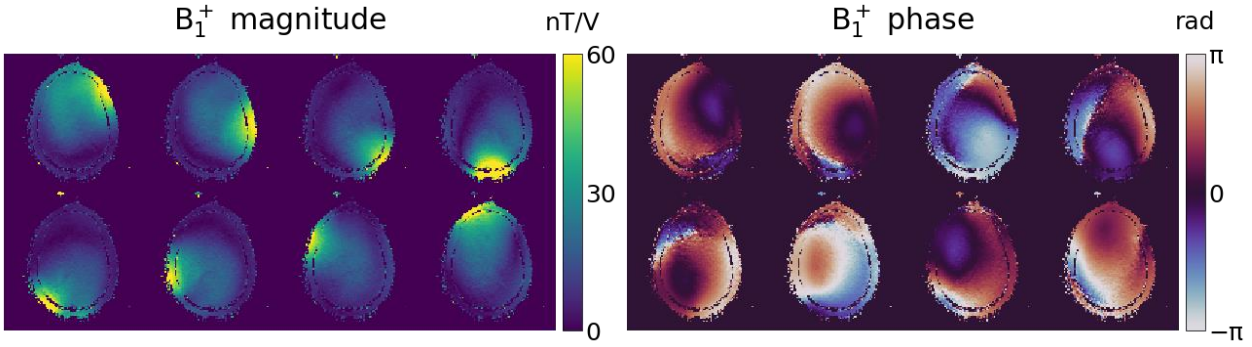

Figure 3.3 Complex B_1^+ distribution produced by an 8 Tx coil in a slice of the brain. B_1^+ mapping was performed using a pre-saturated TurboFLASH sequence. Magnitude values have been rescaled in nT/V (B_1^+ efficiency) and phase values have been rescaled between -π and π.

3.3 Shim weights optimization

Once the N_{Tx} individual B_1^+ maps are stored into a single NIfTI file, they are ready to be loaded by *Shimming-Toolbox* and used to find optimal shim weight values. The optimization of the complex shim weights was the main challenge of this work, as many parameters needed to be accounted for to make it efficient, fast, and suited to the most common B_1^+ shimming scenarios.

3.3.1 Optimization algorithms

The main goal of the optimization process is to find a set w of N_{Tx} complex shim weights that, when combined with the N_{Tx} individual B_1^+ maps, yields an optimal B_1^+ homogeneity across a region of interest. The set of shim weights w therefore has the following structure:

$$w = \begin{bmatrix} \boldsymbol{A_1 e^{i\Phi_1}} \\ \boldsymbol{A_2 e^{i\Phi_2}} \\ \dots \\ \boldsymbol{A_{N_{Tx}} e^{i\Phi_{N_{Tx}}}} \end{bmatrix} = \begin{bmatrix} \boldsymbol{Re_1 + iIm_1} \\ \boldsymbol{Re_2 + iIm_2} \\ \dots \\ \boldsymbol{Re_{N_{Tx}} + iIm_{N_{Tx}}} \end{bmatrix} \tag{3.3}$$

where A_n and ϕ_n are the magnitude and phase values that are applied to the excitation pulse of the n^{th} transmit element, and Re_n and Im_n are the corresponding real and imaginary components.

A commonly used method to find optimal shim weights is to start from a given initial set of shim weights and perform an optimization routine that iteratively modifies the shim weights and uses a specific cost function to evaluate the resulting homogeneity obtained at each iteration. The iterating

process then stop when the cost function cannot be further minimized. The main parameters influencing the final result of this optimization process are therefore the initial set of values (the starting point of the optimization) and the cost function that will be minimized. It is important to note that, in the case of B_1^+ shimming, the shim weights optimization is generally a non-convex optimization problem [78]. This means that, instead of having a single global optimal solution in the $\mathbb{C}^{N_{Tx}}$ space, it may also present several sub-optimal local solutions towards which the optimization is susceptible to converge. This further emphasizes the importance of the initial shim weights used for the optimization, as choosing an initial set of shim weights that is close to the optimal solution maximizes the odds of finding the global minimum of the cost function.

It is also worth noting that in the case of static B_1^+ shimming the number of global minima in $\mathbb{C}^{N_{Tx}}$ is itself infinite, because any phase shift applied simultaneously on all Tx channels will not modify the RF interference pattern (the constructive and destructive interferences will still occur at the same spatial location). However, this infinite number of optimal solutions can be brought down to 1 by setting the phase of the 1st shim weight to 0 and use it as a reference to express the phase values of the following shim weights.

In this work, it was decided to perform the optimization process using the *scipy.optimize.minimize* Python function, a popular and efficient algorithm dedicated to cost function minimization. However, this minimization method works with real variables only, while our shim weights are complex values. A conversion of the set of shim weights w from the complex space $\mathbb{C}^{N_{Tx}}$ to the real space $\mathbb{R}^{2N_{tx}}$ is therefore necessary prior to run the optimization. To do so, the N_{Tx} real and imaginary parts of the initial shim weights are concatenated in a 1D real vector of length $2\times N_{Tx}$ as follows:

$$\begin{bmatrix} \boldsymbol{Re_1} + i\boldsymbol{Im_1} \\ \boldsymbol{Re_2} + i\boldsymbol{Im_2} \\ \dots \\ \boldsymbol{Re_{N_{Tx}}} + i\boldsymbol{Im_{N_{Tx}}} \end{bmatrix} \Rightarrow [\boldsymbol{Re_1}, \boldsymbol{Re_2}, \dots, \boldsymbol{Re_{N_{tx}}}, \boldsymbol{Im_1}, \boldsymbol{Im_2}, \dots, \boldsymbol{Im_{N_{Tx}}}] \qquad (3.4)$$

The choice of splitting the real and imaginary parts of the shim weights rather than their magnitude and phase values was motivated by a comparison of the two methods over a full brain volume. The real/imaginary splitting revealed itself to be up to 30% faster than the magnitude/phase splitting, depending on the number of voxels included in the shimmed ROI, while always converging

towards very close optimal solutions. Some of these observations are reported in Figure 3.4, which compares the B_1^+ shimming results obtained with magnitude/phase and real/imaginary splitting over 20 iterations, in terms of optimization duration (a), coefficient of variation (b), and mean B_1^+ efficiency (c). In this example, the optimization is targeting a B_1^+ efficiency of 30 nT/V in a $64\times64\times40$mm rectangle ROI in the center of a brain volume, using the "target" algorithm that will be described later in this work. This ROI covers 9216 voxels. The real/imaginary splitting is here on average 27% faster than the magnitude/phase splitting, while the mean B_1^+ efficiency and the coefficient of variation remain unchanged.

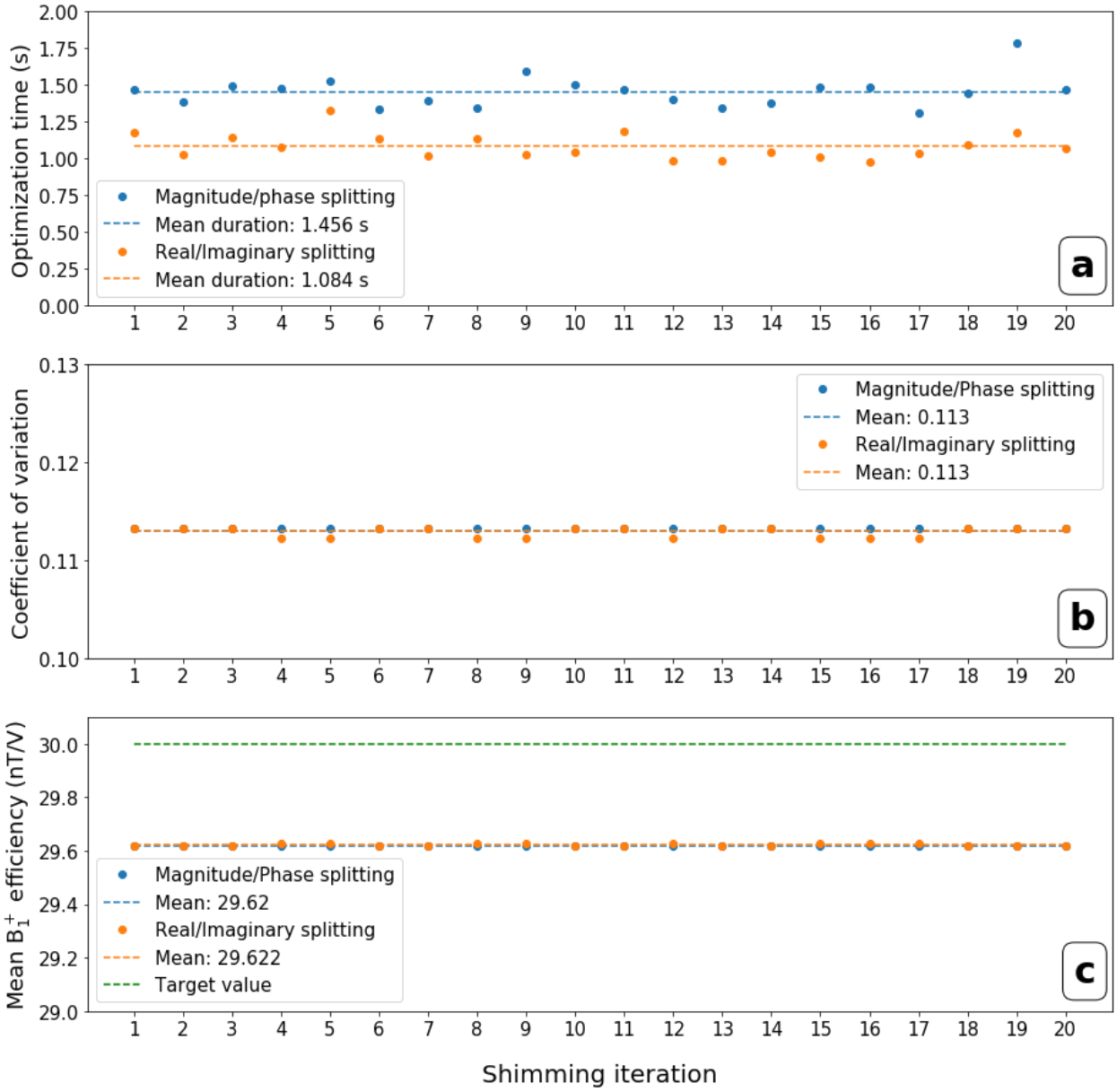

Figure 3.4 Influence of magnitude/phase (MP) vs. real/imaginary (RI) shim weights splitting on the B_1^+ optimization. While they converged toward identical optimal solutions with similar coefficients of variation (B) and mean B_1^+ efficiency (C), RI splitting is on average 27% faster than MP splitting (A). Shim weights optimization was targeting a 30 nT/V B_1^+ efficiency of in a 64×64×40mm rectangle ROI in the center of the brain.

3.3.1.1 Starting point of the complex optimization

Once reshaped into a 1D real vector, the N_{Tx} shim weights can be optimized by the *scipy.optimize.minimize* function.

Regarding the choice of the initial values, the following options have been considered:

1. Starting from a single pulse excitation ($A=1/\sqrt{N_{Tx}}$ and $\phi = 0$ for all Tx element),
2. Starting from the default CP mode values located in the scanners coil files,
3. Starting from a phase-only shimming optimization.

Solution 1 is the easiest to implement, however, the initial shim weights values are very likely to yield a strongly inhomogeneous B_1^+ distribution and may hamper the convergence towards a global minimum by converging towards sub-optimal local minima.

Solution 2 is very likely to start from a homogeneous B_1^+ distribution, as homogeneity is often accounted for when computing the CP mode of a coil. However, this method requires the user to have knowledge of the CP mode shim weights and to input them in a specific text file that could be read by *Shimming-Toolbox*, a time-consuming process, especially for large numbers of Tx elements.

Solution 3 requires an additional optimization step prior to optimize the complex shim weights. For large B_1^+ maps covering a whole brain with 2.5 isotropic resolution, this additional step only takes 0.45s to be performed. It thus ensures to start from an already improved B_1^+ homogeneity while requiring no action from the user and adding negligible additional optimization time. The phase-only optimization is also performed using the *scipy.optimize.minimize()* function but this time only modifying the phase of the shim weights. The phase-only optimization seeks to minimize the coefficient of variation (CV) of the B_1^+ efficiency obtained with a set of N_{Tx} shim phases ϕ as follows:

$$\phi_{phase-only} = \underset{\phi}{argmin}\{CV(|B_1^+(\phi)|)\} = \underset{\phi}{argmin}\left\{\frac{\sigma(|B_1^+(\phi)|)}{\mu(|B_1^+(\phi)|)}\right\} \qquad (3.5)$$

with:

$$B_1^+(\phi) = \sum_n^{N_{Tx}} \frac{1}{\sqrt{N_{Tx}}} B_{1\,n}^+ e^{i\boldsymbol{\phi_n}} \tag{3.6}$$

σ and μ respectively denote the standard deviation and the mean operators.

The choice of minimizing the coefficient of variation (CV) of the B_1^+ efficiency was made because this metric gets rid of the influence of the mean value of a signal (or image) on its homogeneity. This is illustrated by Figure 3.5, where the randomly generated images A and B have the same standard deviation, but a different mean value ($B = A + 5$), and hence a different coefficient of variation. One can observe that, when displayed between 0 and their maximum value, image B is more homogeneous than image A, and this is represented by a lower coefficient of variation. On another hand, image $C = B \times \mu(A)/\mu(B)$ presents the same coefficient of variation as image B. When visually comparing images B and C, they indeed present the same homogeneity. This demonstrates how CV efficiently quantifies the homogeneity of an image as perceived by the human eye. Note that this is only true when the image is displayed ranging from 0 to its maximum. If images A, B, and C were displayed between their minimum and maximum values, they would all look the same. However, in the case of MR images, due to the absence of signal in some spinless regions, the display range usually includes near-zeroed pixels, and CV can be used to quantify the image homogeneity.

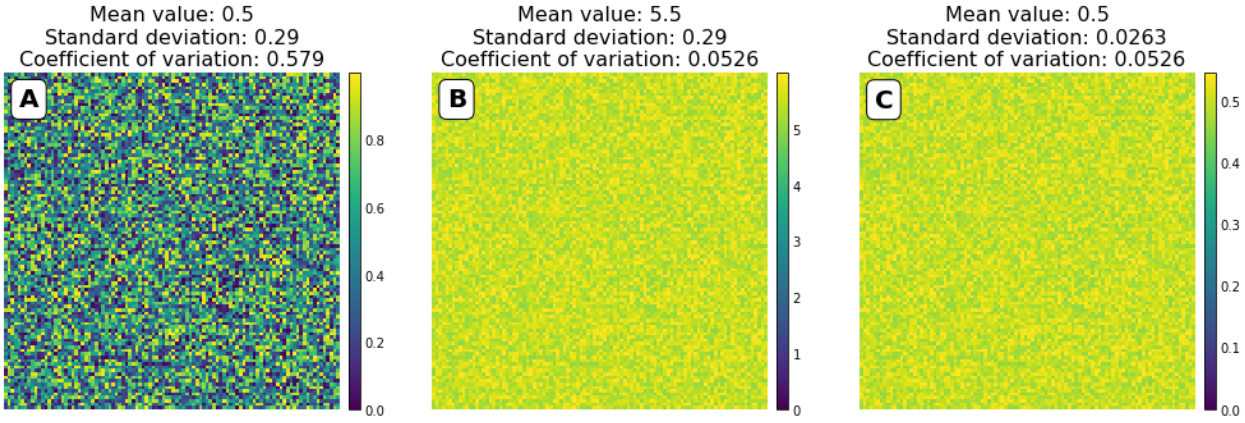

Figure 3.5 Coefficient of variation as a metric for homogeneity. Two images with similar homogeneities (when displayed between 0 and their maximum value) present the same coefficient of variation.

Figure 3.6 shows the B_1^+ efficiencies obtained by combining in-vivo B_1^+ maps acquired over a brain volume with the different shim weights considered as a starting point for optimization. The smaller coefficient of variation associated with the phase-only shimming is a good indicator of an improved homogeneity, as it corresponds to the B_1^+ standard deviation normalized by the mean B_1^+ value. Here, phase-only shimming reduces the B_1^+ coefficient of variation by 47.5% and 8.3% when compared to the single pulse excitation and the pseudo CP mode of the coil, respectively. Note that the CP mode and phase-only shimming resulting distributions are relatively similar. This might be due to the fact that the CP mode has been computed by performing a phase-only shimming on an anatomically similar brain. Note that all the black voxels presented on Figure 3.6 correspond to regions of null signal and are therefore excluded from the optimization process.

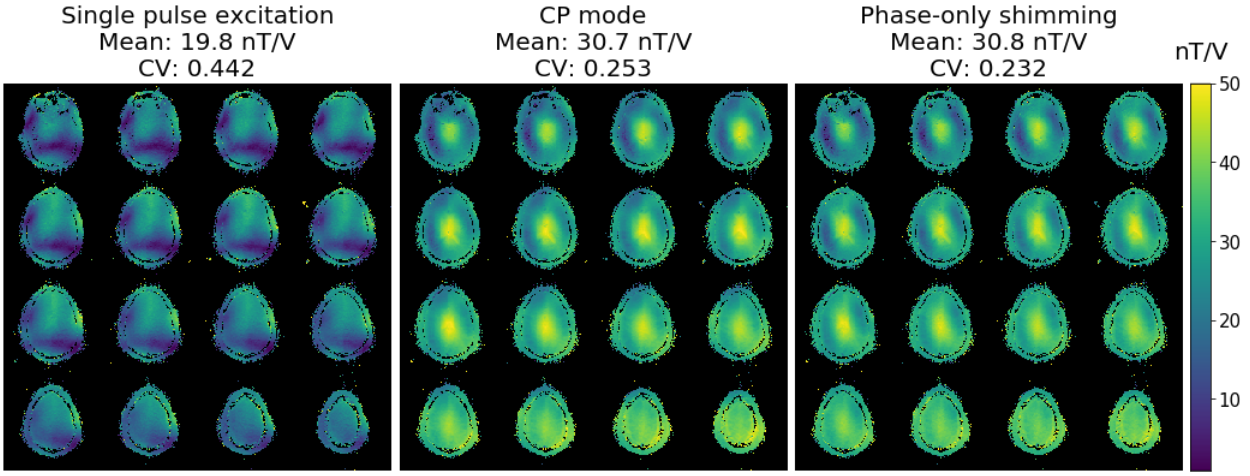

Figure 3.6 B_1^+ efficiencies obtained with the compared initial optimization shim weights. Phase-only shimming results reduce the CV by 47.5% and 8.3% compared to the single pulse excitation and the CP mode, respectively.

Figure 3.7 shows a complex representation of the different sets of shim weights considered as a starting point for the optimization. One can observe that the magnitude of all the shim weights always remains equal to $1/\sqrt{N_{Tx}}$, while their phase values are modified across the different excitation modes.

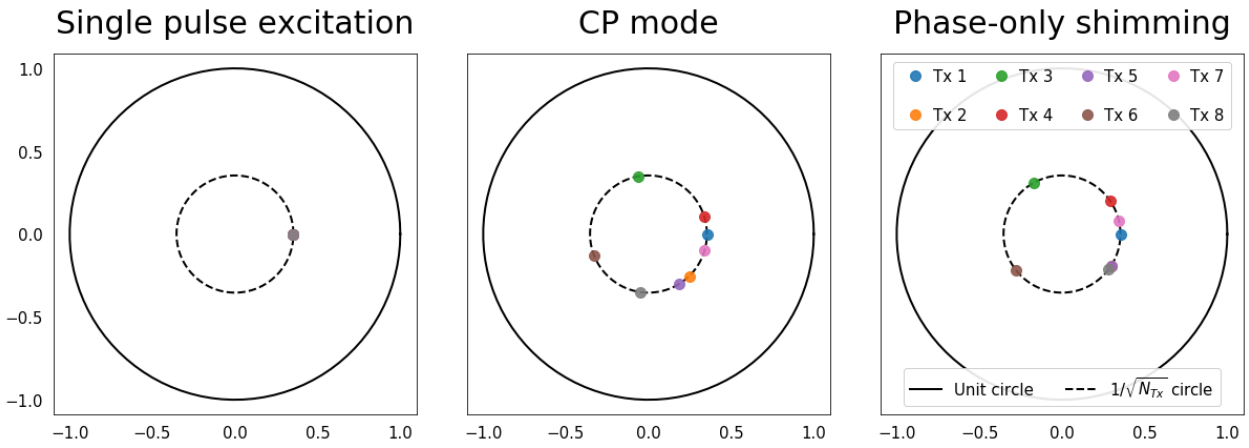

Figure 3.7 Complex visualization of the different sets of shim weights considered as an optimization starting point. X and Y axes correspond to the real and imaginary parts of the shim weights, respectively. The N_{Tx} shim weights of the single pulse excitation are overlapped because they all share the same magnitude and phase values.

From these observations, phase-only shimming was chosen as an optimization starting point, because it does not sacrifice any shimming efficiency and is seamless to the user. Another advantage of the phase-only shimming is that it can be offered as a standalone shimming feature in case some users are only able to adjust the Tx phases on their scanner, for example when they use adjustable hardware phase shifters [15]. This can also be useful for RF coil builders that want to compute a new CP mode for their coil based on in-vivo data rather than simulations.

In order to maximize the odds of converging towards the global cost function minimizer by starting form a good set of phase values, and because the implemented phase-only shimming algorithm is fast, 3 phase-only shimming iterations using randomized initial phases between -π and π are performed prior to optimizing the complex values.

3.3.1.2 Complex shim weights optimization

The next step of the static B_1^+ process is to jointly optimize the magnitude and phase of the shim weights, allowing more degrees of freedom for homogenization. The resulting B_1^+ distribution depends on the cost function that is to be minimized by *scipy.optimize.minimize()*. To cover the most common needs of the B_1^+ shimming community, it has been decided to implement 3 different algorithms, in addition to the phase only shimming solution described above.

The default algorithm was chosen to be the reduction of the coefficient of variation, as its only purpose is to homogenize the B_1^+ efficiency, which is the main application of B_1^+ shimming. The principle is very similar to the phase-only shimming algorithm previously presented, but now the magnitude values of the shim weights are optimized along their phase values, according to

$$w_{CV} = \underset{w}{argmin}\{CV(|B_1^+(w)|)\} = \underset{w}{argmin}\left\{\frac{\sigma(|B_1^+(w)|)}{\mu(|B_1^+(w)|)}\right\} \tag{3.7}$$

with

$$B_1^+(w) = \sum_n^{N_{Tx}} A_n B_{1\,n}^+ e^{i\boldsymbol{\phi_n}} \tag{3.8}$$

and

$$w_n = A_n e^{i\boldsymbol{\phi_n}} \tag{3.9}$$

To prevent the optimization from converging towards null shim weights that would result in a perfectly homogeneous but inexistent B_1^+ efficiency, a regularization parameter is introduced in the cost function to favor solutions resulting in a high B_1^+ efficiency, as it will generally yield a higher signal to noise ratio in the image region of interest. The chosen regularization parameter is the mean B_1^+ efficiency in the shimming ROI divided by 2000. The cost function of equation (3.7) therefore becomes:

$$w_{CV} = \underset{w}{argmin}\left\{CV(|B_1^+(w)|) - \frac{\mu(|B_1^+(w)|)}{2000}\right\} \tag{3.10}$$

The value 2000 was determined empirically by testing the optimization with different available B_1^+ maps and different shimming ROIs, in most cases, this value does not sacrifice any homogeneity (the CV is not modified when compared with unregularized optimization) but yields a higher B_1^+ efficiency and an improved convergence stability. This is illustrated in Figure 3.8Figure 3.1 that compares the results obtained with the unregularized and regularized cost functions across 10 shimming iterations with the example brain B_1^+ maps. Here, the regularized optimization, while 7% faster, results in a similar very similar coefficient of variation (0.047% of difference) and a 9.3% higher mean B_1^+ efficiency. Moreover, the regularized optimization always converges towards the same solution, whereas the 3rd and 9th iterations of the unregularized optimization

converged towards different minima (the optimal CV value is still reached, but the mean B_1^+ efficiency is modified), showing an improved convergence stability with regularization.

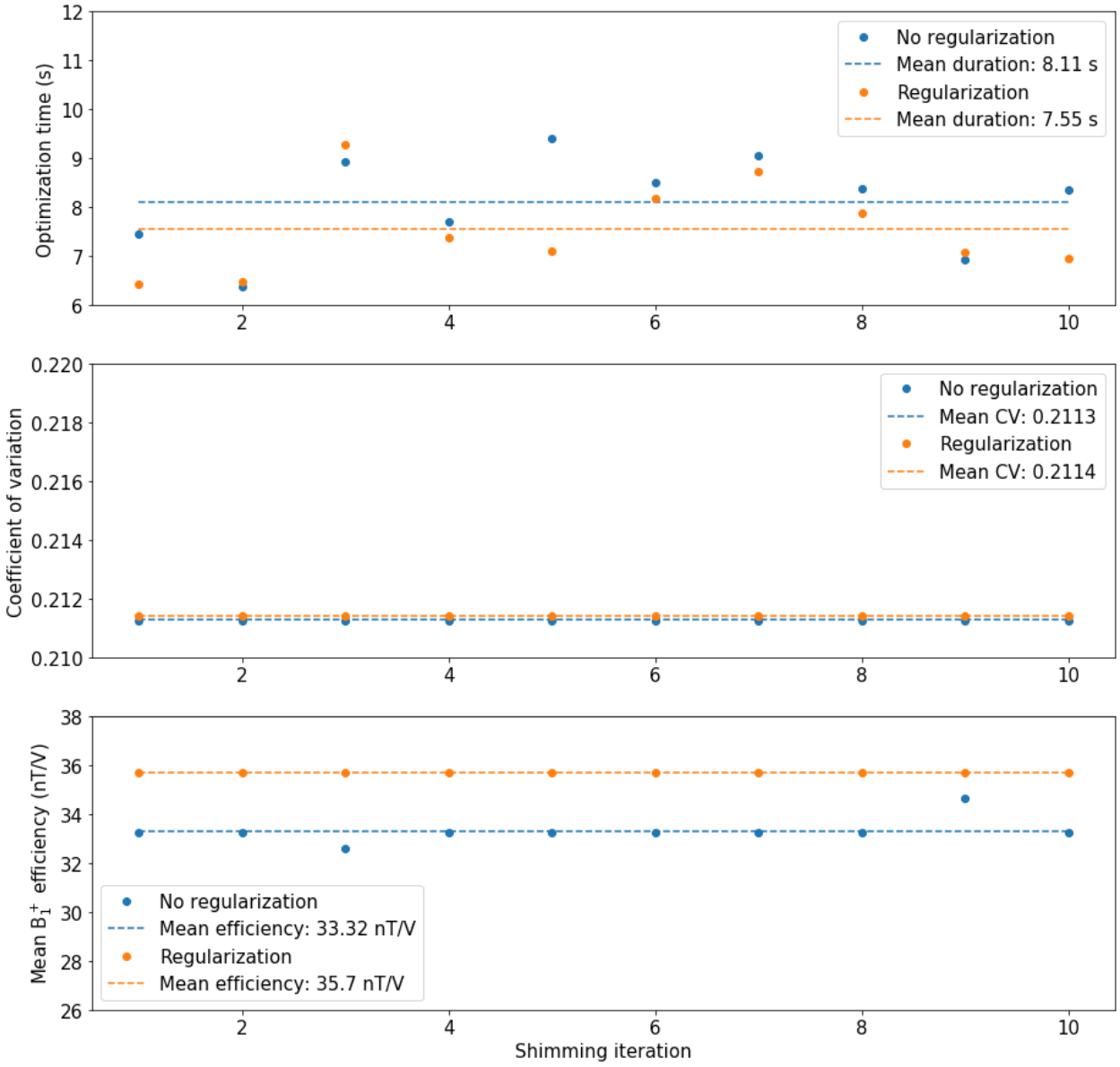

Figure 3.8 Comparison between unregularized and regularized CV reduction. The results of 10 shimming iterations are displayed. While they both converge toward very similar CV values, the regularized optimization is on average 7% faster and yields a 9.3% higher mean B_1^+ efficiency than the unregularized optimization in this example.

Figure 3.9 shows how the CV reduction algorithm compares with single pulse excitation and CP mode over the example brain volume, with a CV reduced by 52.2% and 16.6% respectively.

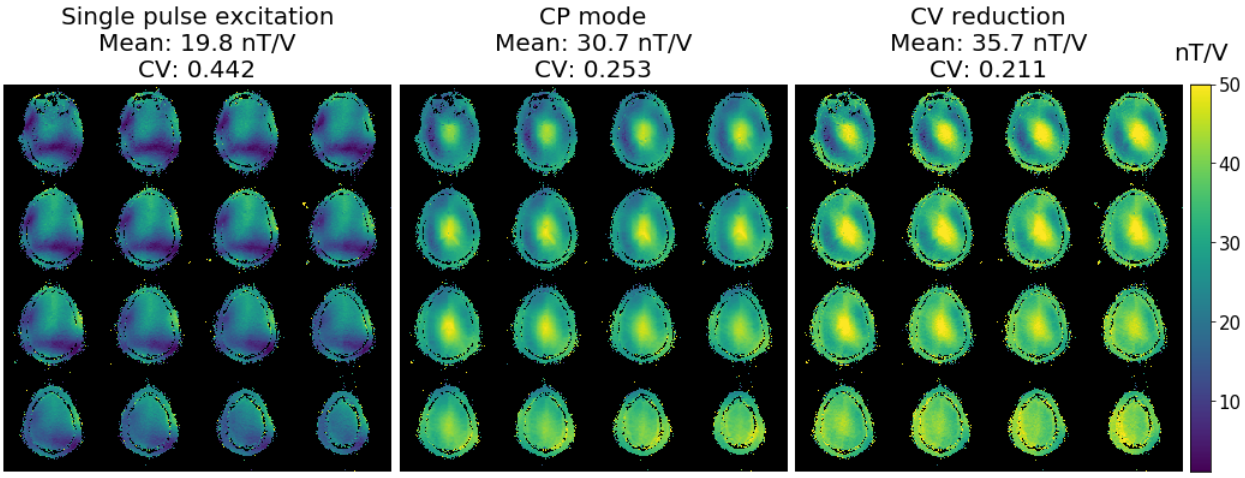

Figure 3.9 B_1^+ efficiency obtained with the CV reduction algorithm compared to single pulse excitation and CP mode, with a respective CV reduction of 52.2% and 16.6%.

Figure 3.10 shows how the shim weights obtained with the CV reduction algorithm compare to the single pulse transmit and CP weights. This time, one can observe that the magnitude values of the shim weights have been modified and are no longer restrained to a circle of radius $1/\sqrt{N_{Tx}}$, illustrating an increased number of degrees of freedom.

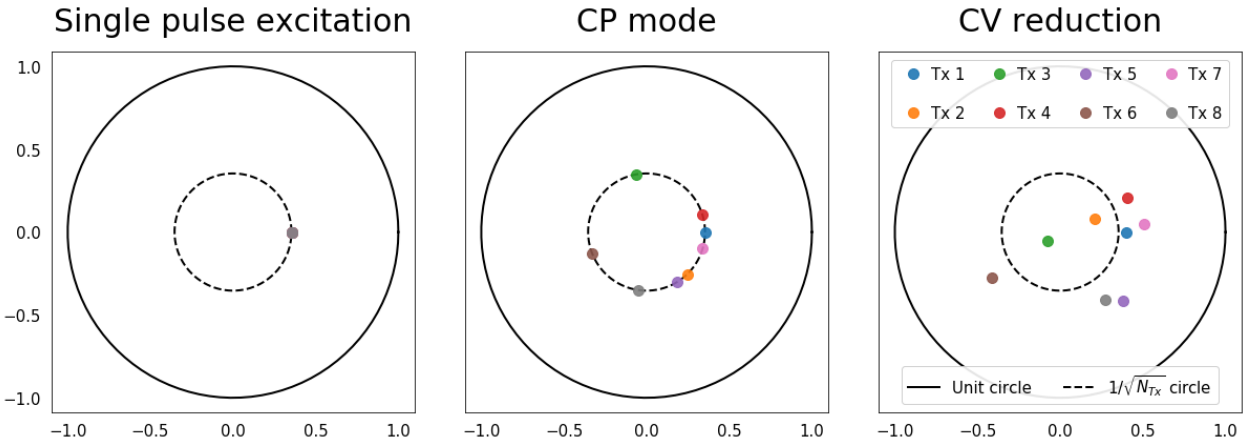

Figure 3.10 Complex visualization of sTx, CP and CV reduction shim weights. With CV reduction, the magnitude values of the shim weights are no longer restrained to a unique value.

The second algorithm, that will be referred to as "target", performs a magnitude least square minimization aiming at reducing the difference between the B_1^+ efficiency and a target value t specified by the user over all voxels of interests, according to the following cost function:

$$w_{target} = \underset{w}{argmin}\left\{\sum_{n}^{N_{voxels}} (|B_1^+(w)| - t)^2\right\} \quad (3.11)$$

In this scenario, if the target value is low enough, it can be reached without sacrificing any homogeneity compared to the CV reduction algorithm: the optimal shim weights are simply linearly rescaled to approach the target value. However, if the target value is too high to be reached without exceeding the optimization bounds, some homogeneity is sacrificed to obtain a higher B_1^+ efficiency. This is illustrated by Figure 3.11 that shows how a target of 30 nT/V results in the same homogeneity as the CV reduction algorithm shown on Figure 3.9, and how the coefficient of variation increases when the target value becomes too high to be reached. The target algorithm can notably be useful when the user wants to keep a constant B_1^+ field over different iterations of an experiment or across the different subjects of a study to make sure that the resulting images were acquired with similar flip angles.

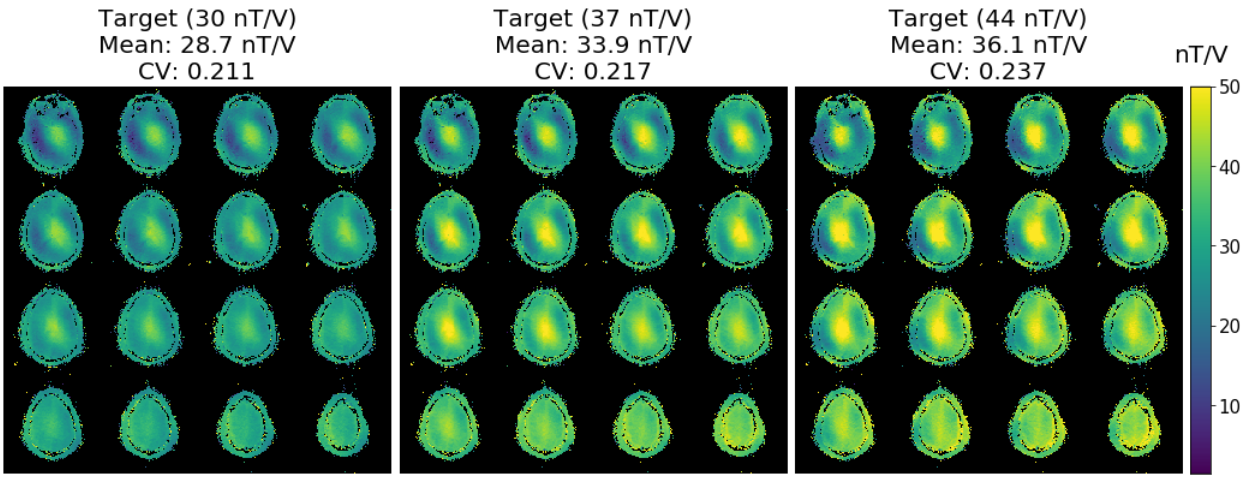

Figure 3.11 B_1^+ efficiency obtained with the target algorithm when increasing the target value. The CV increases when the targeted B_1^+ efficiency becomes too high to be reached while keeping an optimal homogeneity.

The last proposed algorithm seeks to maximize the SAR efficiency (or safety excitation efficiency), defined as the ratio of the mean B_1^+ efficiency and the square root on the maximum local SAR value [79]. The cost function associated to this algorithm is as follows:

$$w_{SAR_{eff}} = \underset{w}{argmin}\{SAR_{eff}(w)\} \tag{3.12}$$

with

$$SAR_{eff}(w) = \frac{\mu(|B_1^+(w)|)}{\sqrt{max(SAR_{local}(w))}} \tag{3.13}$$

This optimization is of interest to users seeking to get a high signal in a specific region of interest while keeping the local energy deposition low to ensure patient safety. However, unlike the other proposed algorithms, it does not seek to homogenize the B_1^+ efficiency. The results obtained with SAR efficiency shimming are compared with the other algorithm in Figure 3.12. As expected, SAR efficiency shimming results in a high mean B_1^+ value but, for a region of interest as large as the brain, it also results in local hotspots and dark regions, making SAR efficiency shimming better suited to applications looking for a strong B_1^+ in a spatially limited region where the signal would otherwise likely be low.

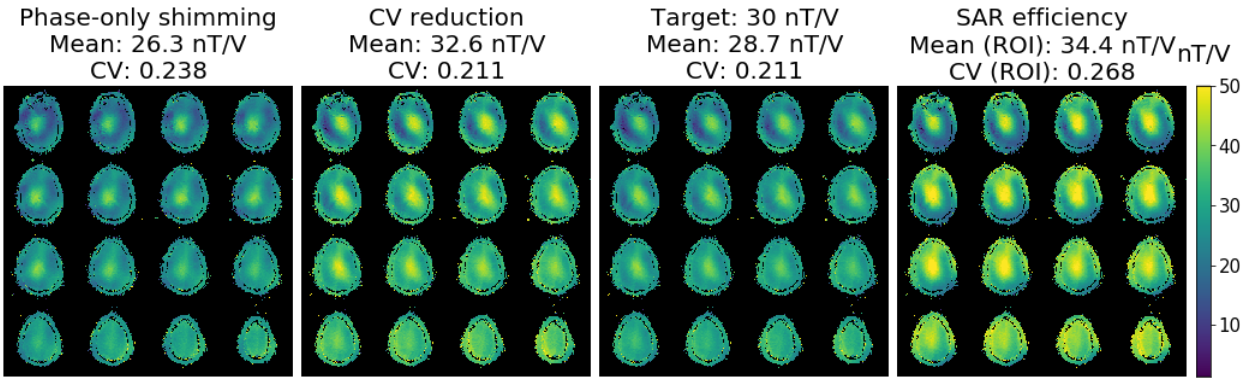

Figure 3.12 B_1^+ distributions obtained with the 4 implemented algorithms.

Figure 3.13 shows the shim weights obtained with the different implemented algorithms. One can note here that the target algorithm yields a rescaling of the CV reduction shim weights. This is because the 30nT/V target value is still in the range that allows for an optimal CV.

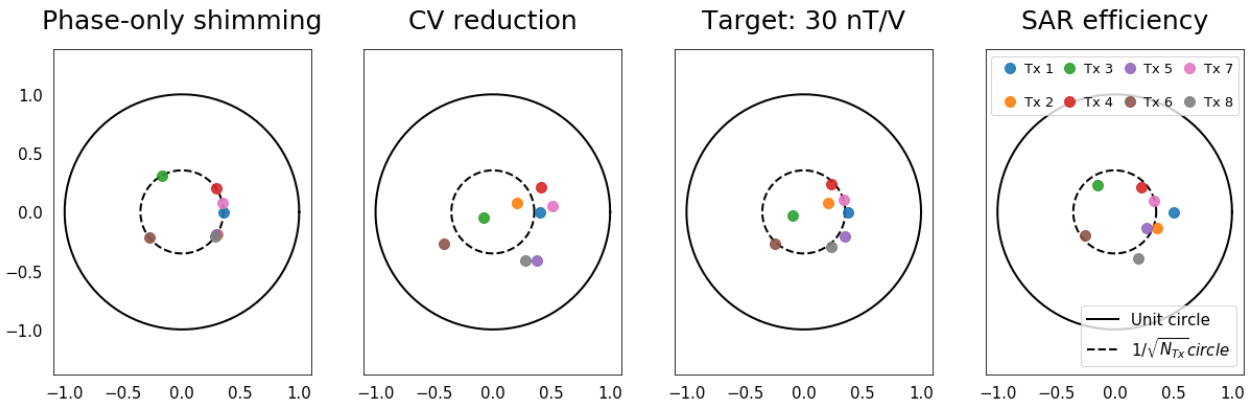

Figure 3.13 Complex shim weights resulting from the 4 implemented algorithms.

In the end, when performed on our in-vivo brain example, which is a large region compared to what is expected to be shimmed over in most applications, all the implemented optimization methods summed up in Table 3.1 require less than 10s on a laptop with average 2022 specifications, which is negligible compared to the time needed to transfer the data from the scanner to the computer running *Shimming-Toolbox*, to perform the conversion and the optimization process, and to input the shim weights on the scanner. However, no tests have been performed with a larger number of Tx elements because of the non availability of such data. In this scenario, the optimization time could however become significantly longer.

Table 3.1 The B_1^+ shimming algorithms implemented in *Shimming-Toolbox*

Algorithm	**Phase-only**	**CV reduction**	**Target**	**SAR efficiency**
Goal	Find a set of phase values $\boldsymbol{\phi}$ that homogenize B_1^+ efficiency	Find a set of complex shim weights $\mathbf{w}$ that homogenize B_1^+ efficiency	Target a B_1^+ efficiency value $\mathbf{t}$ set by the user	Maximize the mean B_1^+ efficiency to maximum local SAR ratio
Cost function	$\frac{\sigma(\lvert B_1^+(\phi)\rvert)}{\mu(\lvert B_1^+(\phi)\rvert)}$	$CV(\lvert B_1^+(w)\rvert) - \frac{\mu(\lvert B_1^+(w)\rvert)}{2000}$	$\sum_n^{N_{voxels}} (\lvert B_1^+(w)\rvert - t)^2$	$\frac{max(SAR_{local})}{\mu(\lvert B_1^+(w)\rvert)}$

3.3.2 Constraining the energy deposition

When running an MRI sequence, the scanner monitors the energy deposition by computing the SAR values. If the SAR limits set by the IEC are exceeded, the sequence is interrupted, and the images cannot be reconstructed. At this point, the scanner may offer the possibility to run the sequence with an increased repetition time, making it slower but reducing the SAR, or to use the first level controlled operating mode which fixes a higher limit for local SAR but may cause physiological stress to the patient. Both these scenarios are to be avoided as they result in wasted scan time.

On the 7T Magnetom Terra scanner, SAR is computed from compressed Q matrices called virtual observation points (VOP) stored in a MATLAB (.mat) file in the scanner file system. Each RF coil that was made compatible with the scanner must have its corresponding VOP file. As this file is accessible to any person running the scanner, it was decided that it would be used by *Shimming-Toolbox* to compute the SAR values during the shim weights optimization. A Python function has thus been implemented to read in the .mat file and extract the VOP matrices so that they can be used to constrain the maximum SAR value during the optimization. To allow more flexibility for the optimization process, and thus better homogenize B_1^+, a SAR factor is introduced to set the maximum local SAR limit after B_1^+ shimming to SAR_{factor} times the maximum local SAR obtained with a phase-only shimming. By default, the SAR_{factor} is set to 1.5, as it was empirically found to work well with the most popular imaging sequences, without sacrificing much homogeneity. Note that the SAR factor should always remain greater or equal to 1, otherwise the initial optimization conditions (the phase only shim weights) will exceed the SAR limit. The influence of the SAR factor over the CV reduction algorithm is illustrated by Figure 3.14 that shows how an increase of the SAR factor allows for a higher mean B_1^+ efficiency, while still preserving an optimal homogeneity. One can observe than the relation between SAR factor and mean B_1^+ efficiency is not linear.

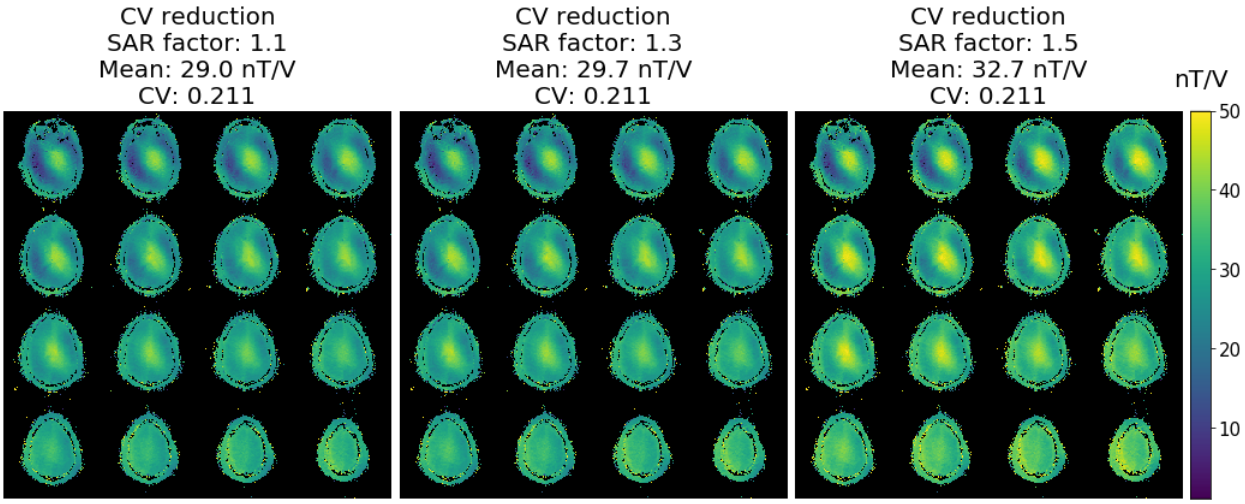

Figure 3.14 Influence of the SAR factor over the CV reduction optimization. Less constraints on the maximum local SAR result in higher mean B_1^+ efficiencies while the CV remains the same.

In the scenarios where, for any reason, no VOP are provided by the user to compute the maximum local SAR value, it is still possible to perform the optimization (except for the SAR efficiency shimming algorithm). In these cases, a constraint is applied on the Euclidean norm of the shim weights so that it remains equal to 1 during the optimization. A norm of 1 is what is used for the CP mode, where the magnitude of the pulses sent to each Tx element is $1/\sqrt{N_{Tx}}$. The maximum local SAR obtained when applying the shim weights is thus expected to be of the same order of magnitude as the maximum local SAR obtained with the CP mode and should not result in a SAR excess at the scanner. However, as no direct SAR estimation is performed in this scenario, there is no way to make sure that the optimized shim weights will not induce SAR hotspots at some locations.

As constraints are now applied on the nonconvex optimization problem, *scipy.optimize.minimize* calls a Sequential List Square Programming implementation for cost function minimization [80].

Note that, even with a constraint on the RF energy deposition, there is still a possibility to exceed the safety limits at the scanner when running high SAR sequences, just as it might happen with the default CP mode or any other excitation mode. If this occurs, it will be up to the user to modify the imaging parameters (e.g., increase the repetition time) or change the safety control level so that the sequence may be completed.

3.4 Shimming over segmented regions

On all the shimming results presented so far, one can still observe local B_1^+ hotspots, even after shimming. This is mainly due to the limited number of degrees of freedom available for homogenization. By reducing the number of voxels over which one wants to shim, the optimal homogeneity that can be reached over this reduced region of interest will be improved. Another benefit of including fewer voxels into the optimization pipeline is that it makes it faster. However, by homogenizing over a limited ROI, one takes the risk of increasing the inhomogeneity in the rest of the image. This is therefore only suitable for applications where the researcher or clinician is interested in a small portion of the image. Examples of B_1^+ shimming applications targeting specific anatomical regions such as the cerebellum [81], the hip [54], the liver [82] or the prostate [15] can be found in literature, reflecting an interest of the MRI community for these applications.

Figure 3.15 illustrates how shimming over a reduced ROI results in a more accurate control of the B_1^+ efficiency and a lower field variation. The brain segmentation presented in the middle panel was performed on an anatomical gradient echo image with the *Brain Extraction Tool (Analysis Group, FMRIB, Oxford, UK).* While using the target algorithm over a segmented brain slightly improves the homogeneity and the proximity to the 30nT/V target, using a 64×64×40mm rectangle ROI (right) further approaches the target value and significantly reduces the CV.

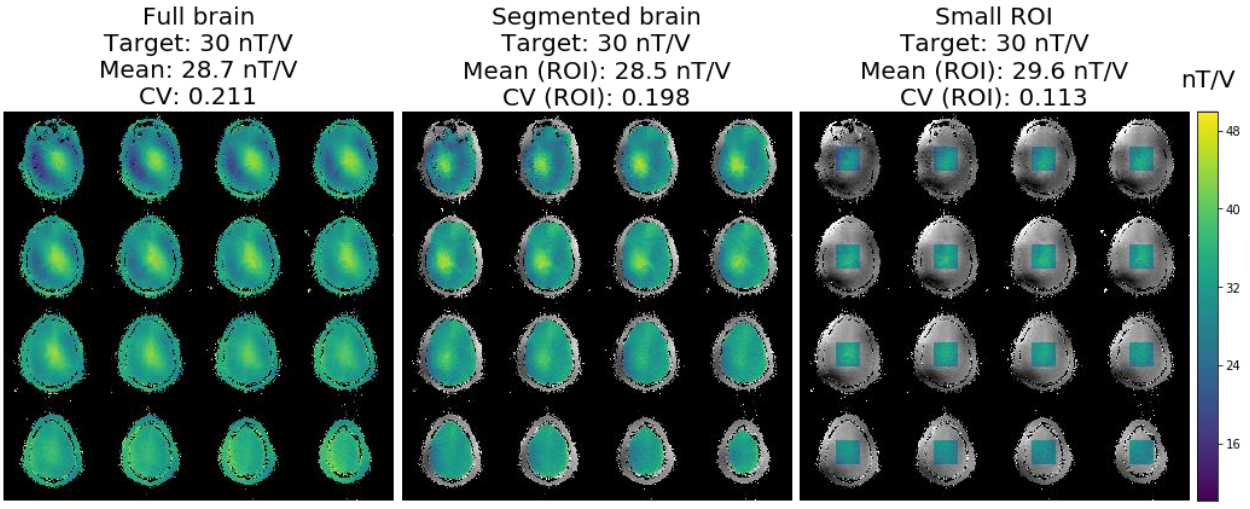

Figure 3.15 Influence of the ROI size over the homogenization. Reducing the ROI size results in lower CV values in the region of interest and a better control over the mean B_1^+ efficiency.

To allow the user to perform B_1^+ shimming over specific anatomical regions, it was necessary to make *Shimming-Toolbox* compatible with external segmentation software. As many popular open-access segmentation libraries already handled NIfTI files, the main challenge here was to make sure that the segmented ROI would be correctly applied to the B_1^+ volume, even if it was acquired with a different resolution, orientation or FOV. To this end, the segmentation volume is resampled into the B_1^+ volume using a spline interpolation implemented as part of NIPY's *Nibabel*, a Python library dedicated to the processing of medical and neuroimaging file formats. Once the two volumes are resampled and present the same voxel grid, all the B_1^+ voxels located outside of the segmented region are excluded from the shim weights optimization.

For users that desire to shim over a specific region but don't want to use external segmentation tools, *Shimming-Toolbox* offers the possibility to create rectangle masks with different positions and sizes. A thresholding masking option that removes all low signal voxels from a selected volume is also available. When no mask is provided by the user, all non-null voxels of the B_1^+ volume are included in the optimization process.

3.5 Output files

Once the shim weights optimization is complete, they are stored in a text file created in the output folder specified by the user. Figure 3.16 is an example of such text file, obtained after performing B_1^+ shimming for a coil with 8 Tx elements.

Channel	mag	phase (°)
Tx1	0.116	0.000
Tx2	0.405	-99.537
Tx3	0.319	17.631
Tx4	0.759	158.577
Tx5	0.531	2.592
Tx6	0.416	163.813
Tx7	0.093	81.387
Tx8	0.351	-92.824

Figure 3.16 Output text file containing the optimized shim weights for 8 Tx elements.

Once the user gets this text file, the next step is to manually input these optimized magnitude and phase values into the scanner's console so that they can be applied during the following acquisition. This process is cumbersome and takes about 1 minute for an 8 Tx elements array (and a proportionally increasing amount of time for higher number of Tx channels). However, no better solution has been found so far to automatically bypass the use of the default CP mode weights without the need for sequence programming that would make our B_1^+ shimming implementation only compatible with a few pre-adapted sequences.

Along this text file are also provided a .png image showing the B_1^+ efficiency distribution in the imaged volume, and a pair of NIfTI/JSON files corresponding to the shimmed B_1^+ volume. These files are mostly useful to assert that the optimization behaved as expected before inputting the shim weights on the console.

3.6 Graphical user interface

In an effort to make the use of *Shimming-Toolbox* fast, intuitive, and appealing, it was decided to develop a Graphical user interface (GUI) that gathers all the implemented features in a dynamic and easy to navigate environment. Rather than creating a GUI from scratch, the choice was made to propose a plugin for *FSLeyes*, a pre-existing and widely used medical imaging interface developed by Paul McCarthy (University of Oxford). This choice was motivated by the many features already offered by *FSLeyes*, such as the handling of NIfTI files, the dynamic visualisation of 3D volumes, and the integration of various image processing software (e.g., segmentation tools). Moreover, *FSLeyes* is an open access software and, as such, does not limit the range of potential *Shimming-Toolbox* users.

The graphical plugin was implemented using *wxPython*, the library that was used for developing *FSLeyes*. The current GUI implementation is presented in Figure 3.17, that shows the *Shimming-Toolbox* plugin along with *FSLeyes*' 3D viewer. All B_1^+ shimming features are gathered in a single tab, and a dropdown menu enables to switch between the different algorithms. To guide the user through the shimming process, information buttons describing the different inputs and outputs are provided and asterisks are used to mark the mandatory input fields.

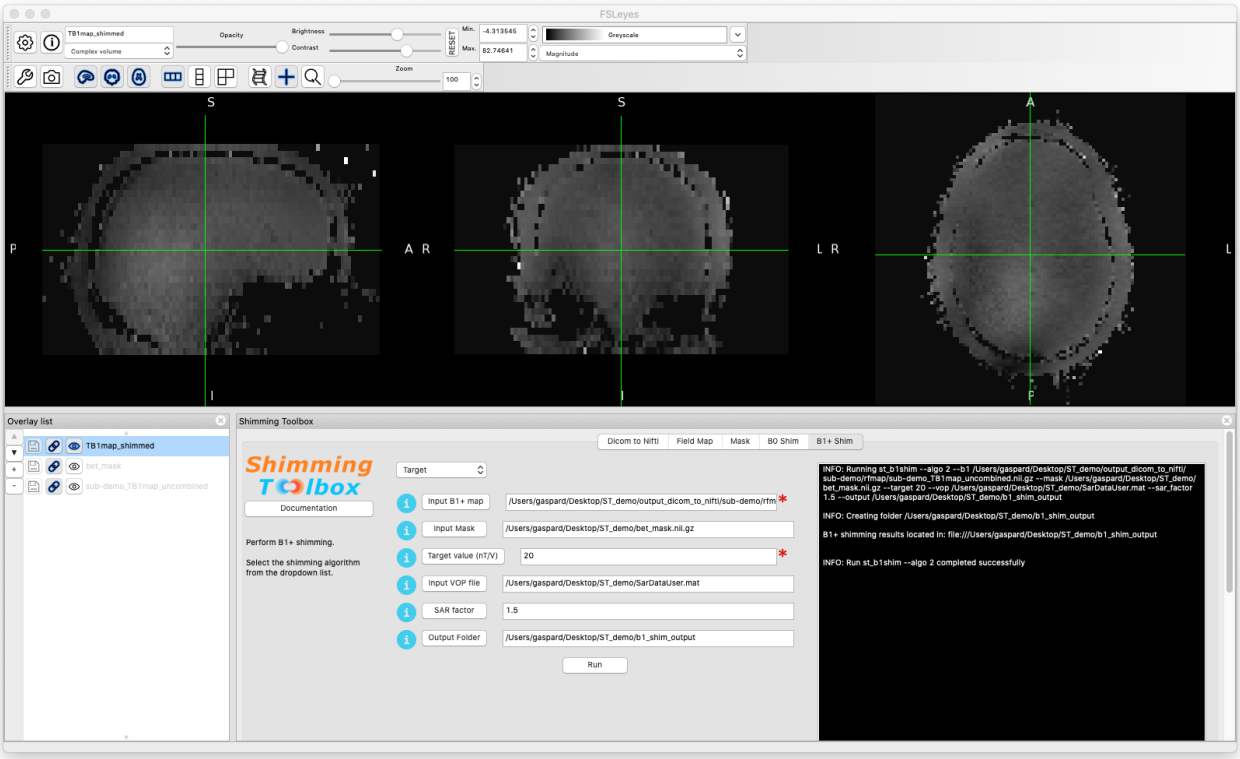

Figure 3.17 Integration of *Shimming-Toolbox* into the *FSLeyes* GUI. The last tab of the plugin is dedicated to B_1^+ shimming.

CHAPTER 4 STATIC B_1^+ SHIMMING IN THE SPINAL CORD

This chapter focuses on the evaluating the benefits of in-vivo static B_1^+ shimming for spinal cord imaging applications at 7T.

4.1 Context of the study

As part of the central nervous system, the spinal cord is what connects the brain to the extremities of the body, thus serving a major role for motricity and sensing. Spinal cord imaging therefore has a strong clinical impact as it allows for a detection of spinal cord injuries and pathologies that may drastically affect the patient's physical abilities. MRI being particularly good at imaging soft tissues, it is a well suited imaging modality for visualizing the small structures composing the spinal cord, and it highly benefits from the improved resolution and contrast associated with UHF imaging [9], [21].

Custom spine coils for UHF MRI with pTx capability have been developed and tested by various research teams around the world [9], [19]–[24], motivating the evaluation of the benefits of patient-specific B_1^+ shimming within the spinal cord. The spinal cord is a particularly challenging region to image due to anatomical properties such as its depth in the body or its extent in the head-foot direction, we therefore expect B_1^+ shimming to significantly improve the image homogeneity in the spinal cord at UHF, as a better control over the B_1^+ field may help overcome these challenges.

In this work, we study how patient-specific B_1^+ shimming can be used to improve the image homogeneity along the cervical and thoracic spinal cord at 7T, using a custom 8Tx-20Rx spine coil array.

4.2 Methods

4.2.1 Scanner and coil

For this study, all acquisitions were performed on a 7T Magnetom Terra scanner (Siemens, Erlangen, Germany). An improved version of a previously presented custom Tx-Rx cervical spine coil [23] was used. The coil is composed of a transmit-only array of 8 dipoles irregularly placed around the subject, and a receive-only array consisting of 20 circular loops (15 loops are placed

under the subject's head/neck and 5 are placed on the anterior region of the neck). The positions of all the RF elements are presented in Figure 4.1. Top panel (A) shows the positions of the 8 transmit dipoles. Bottom panel (B) shows the position of the 20 receive loops. This coil was designed to provide a field-of-view covering from the occipital lobe to the mid-thoracic spine.

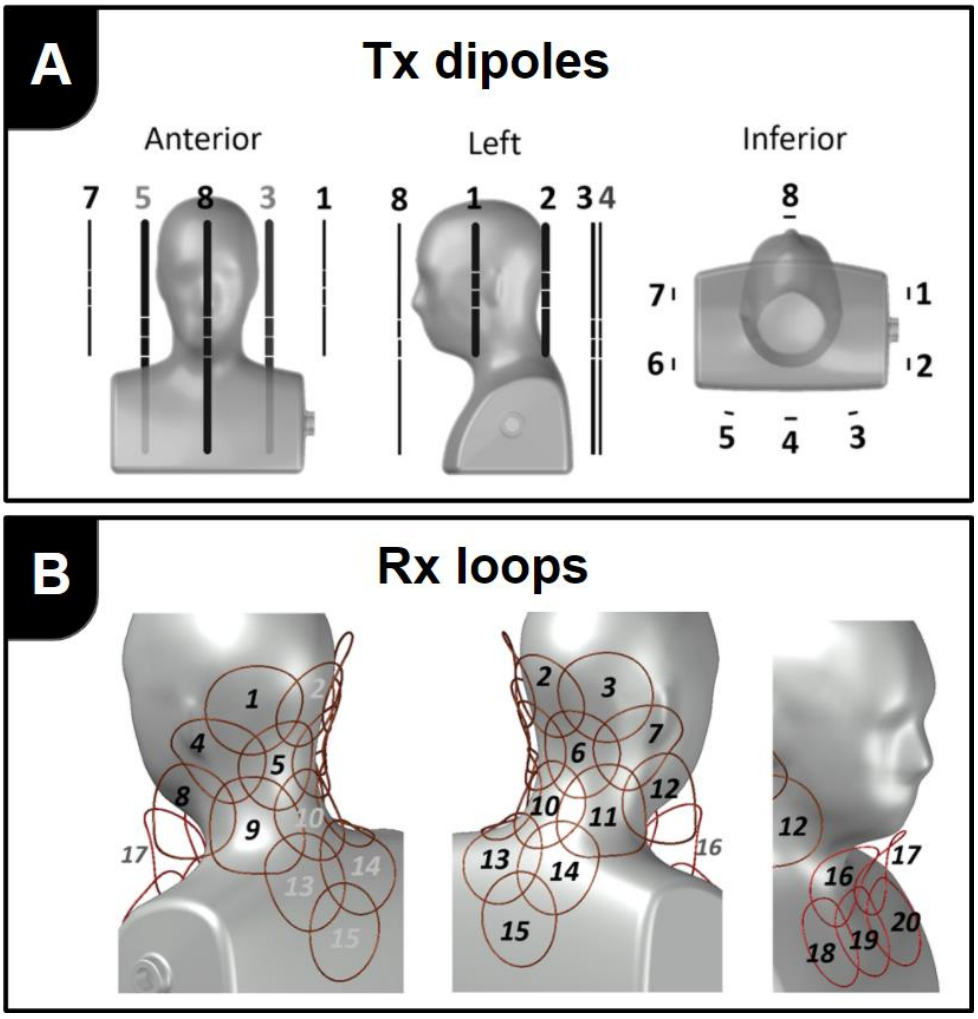

Figure 4.1 Custom coil geometry: positioning of the RF elements. 8 transmit dipoles (a) and 20 receive loops (b) are placed around the patient.

All in-vivo scans performed in this study were approved by the ethics committee of the scanning site, and written consent was obtained from all subjects.

4.2.2 Acquisition of the unshimmed anatomical volumes

Unshimmed volumes were acquired using the coil's default circular polarization (CP) mode which was computed from in-vivo B_1^+ maps acquired in one subject. The CP mode phase values were determined by setting all individual B_1^+ fields produced by each Tx element in phase in a voxel located in the spinal cord at the C2-C3 level, resulting in a strong B_1^+ field in the cervical region due to constructive RF interferences. This excitation mode is thus optimized for imaging applications focused on the cervical spine, but results in an overall inhomogeneous B_1^+ distribution when including the thoracic region. As a non-patient-specific excitation mode, it also does not account for inter-subject anatomical variations.

A MP2RAGE sequence [83] was used to acquire a 256x224x192 mm sagittal volume with a 1mm isotropic resolution for a total acquisition time 247s with a repetition time of 3.25s and an echo time of 1.83ms. The reference voltage was fixed to 400V for all scans and participants due to hardware limitations.

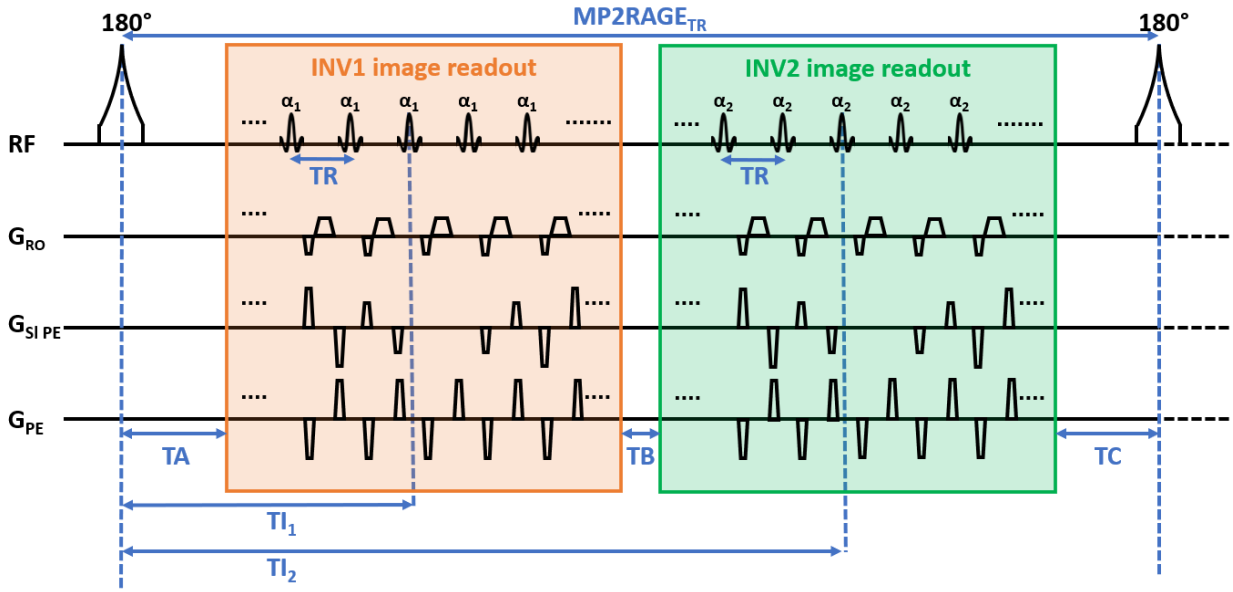

Figure 4.2 Diagram of the MP2RAGE sequence. INV1 and INV2 images are respectively acquired with inversion times TI_1 and TI_2 (time from the middle of the inversion pulse to the excitation of the k-space phase encoding center line in the slab selection direction). Adapted from *Marques et al. 2010* [83].

As part of this MP2RAGE sequence, two GRE volumes (INV1 and INV2) with different inversion times (TI_1=0.84s, TI_2=2.37s) and flip angles (FA_1=5°, FA_2=6°) were acquired and used to compute a uniform T_1 weighted image (UNI) [84] as follows:

$$UNI = \frac{INV1 \times INV2^*}{INV1^2 + INV^2} \quad (4.1)$$

UNI images are interesting for assessing the benefits of B_1^+ homogenization, as they are not subject to B_1^-, T_2^* and proton density inhomogeneities, but do not completely get rid of B_1^+ inhomogeneity effects [83].

4.2.3 B_1^+ mapping

As discussed in the previous chapter, patient-specific B_1^+ shimming requires knowledge of the B_1^+ distribution produced by each Tx element within the shimming region of interest. In this study, uncombined complex B_1^+ maps were acquired using the already discussed pre-saturation-based Turbo FLASH B_1^+ mapping sequence [77]. This sequence is particularly fast, as it requires 64s to get individual sagittal B_1^+ maps over a $240\times388\times84$mm FOV with a $2\times2\times3.6$mm resolution. As no abrupt variation of the B_1^+ efficiency in the spinal cord was observed, this fairly low resolution was deemed sufficient to efficiently shim and to make the B_1^+ mapping fast. For all experiments, the flip angle was set to 90° for the saturation pulse and 10° for the imaging pulse. The echo time was 1.79 ms, the repetition time was 6.97 s, the bandwidth was 555 Hz/px, and the reference voltage was 400 V.

4.2.4 Static B_1^+ shimming focused on the spinal cord

As the ROI size affects the B_1^+ shimming efficiency [55], we aimed at homogenizing the B_1^+ field in the spinal cord only. To this end, a segmentation of the spinal cord was performed using the Spinal Cord Toolbox [85], and used as a mask for B_1^+ shimming. Segmentation was performed on the 1mm isotropic INV2 GRE images acquired as part of the MP2RAGE protocol. The INV2 images were chosen for segmentation because they resulted in more accurate segmentations when compared to INV1 and UNI images during preliminary tests.

The shim weights optimization was performed with *Shimming-toolbox*, using the "target" algorithm presented in the previous chapter. The targeted B_1^+ efficiency was set to 15 nT/V and a SAR factor of 1.5 was used to constrain the maximum local SAR. The target value of 15 nT/V was chosen because it was experimentally observed to be reachable without SAR excess for different subjects.

Optimized shim-weights were then manually input on the scanner's console and applied to the exact same MP2RAGE sequence that was used to acquire the unshimmed images. The total duration of the whole B_1^+ shimming process is on the order of 5 to 10 minutes.

As we aim to evaluate the homogeneity improvement in the same anatomical region of the spinal cord before and after shimming, shimmed and unshimmed images were manually segmented, and co-registered. CV values were then computed over the voxels segmented on the unshimmed images. As a consequence, this tends to underestimate the efficiency of the B_1^+ shimming in case of mismatches in the registration process, because some voxels located outside of the spinal-cord could be including in the ROI and affect the CV value, especially on UNI images that are more homogeneous than INV2 images in the spinal-cord.

4.3 Results

4.3.1 Efficiency of the target algorithm in the segmented spine

Figure 4.3 compares the total B_1^+ efficiency obtained when combining individual B_1^+ maps acquired in-vivo with the CP mode weights (a) and the optimized shim weights (b). A single slice located in the center of the spine is displayed for clarity, but the reported values correspond to the whole segmented spinal cord (colored region) over which the shimming was performed. It shows how the B_1^+ shimming algorithm efficiently homogenizes the B_1^+ field in the spinal cord. Indeed, when compared to the CP mode that yields high B_1^+ values in the cervical spine and low B_1^+ values in the thoracic region, the shimmed values exhibit a 66.7% smaller coefficient of variation (CV) along the segmented spinal cord, resulting in a homogeneous B_1^+ field with reduced dispersion around the 14.98 nT/V mean B_1^+ value (for a target value of 15 nT/V). Figure 4.4 shows similar

improvements obtained with the exact same experiment for another scan subject. This time, B_1^+ shimming results in a 61.7% CV decrease in the segmented spinal cord.

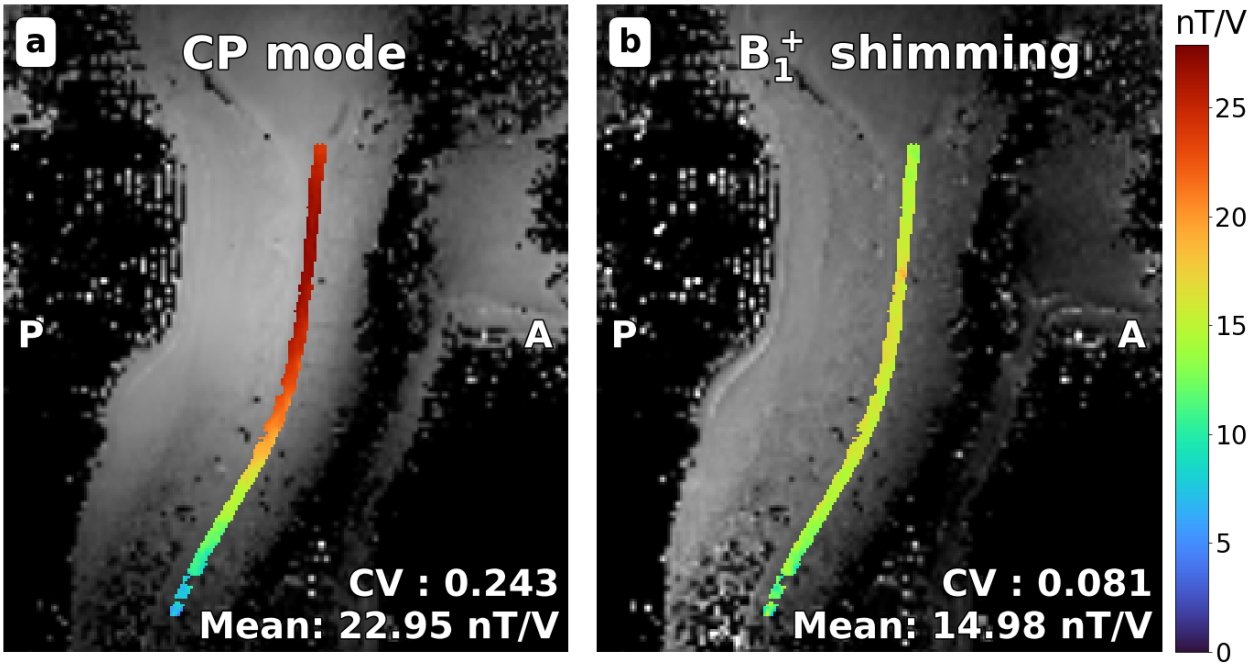

Figure 4.3 In-vivo B_1^+ maps with CP mode and optimized shim weights (subject 1). The colored voxels correspond to the automatically segmented spinal cord used as a B_1^+ shimming ROI. A value of 15nT/V was targeted by the shimming algorithm. After shimming, the CV in the ROI is reduced by 66.7%.

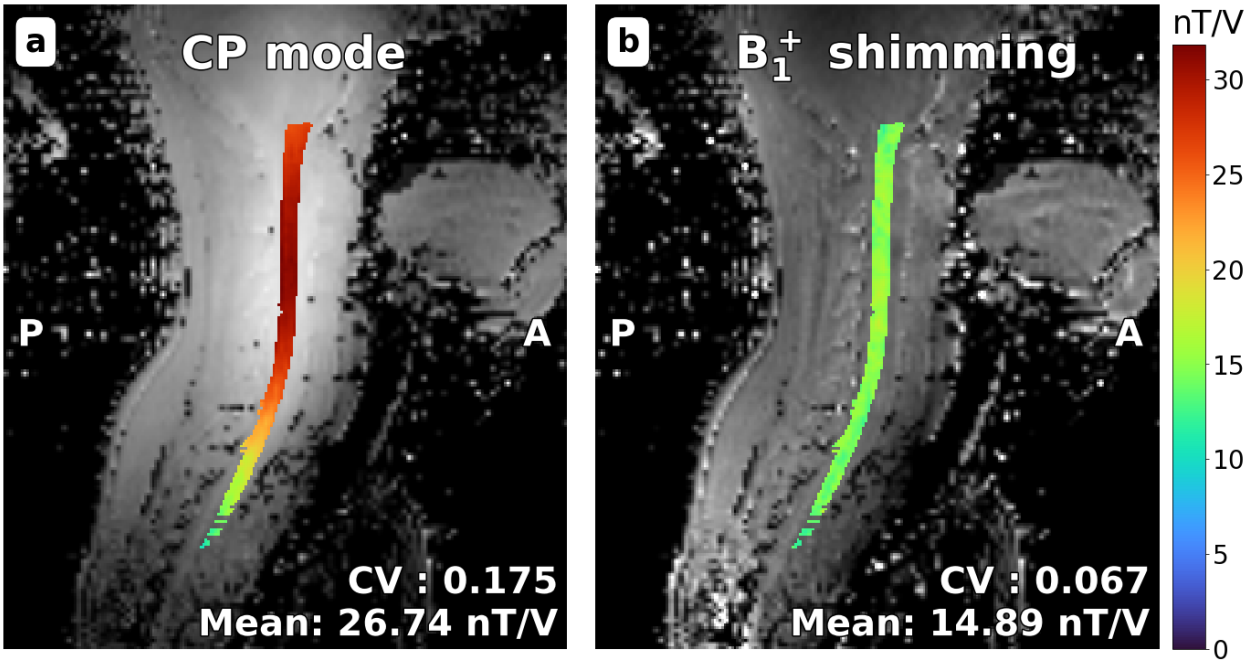

Figure 4.4 In-vivo B_1^+ maps with CP mode and optimized shim weights (subject 2). The colored voxels correspond to the automatically segmented spinal cord used as a B_1^+ shimming ROI. A value of 15nT/V was targeted by the shimming algorithm. After shimming, the CV in the ROI is reduced by 61.7%.

The CV reductions shown on Figure 4.3 and Figure 4.4 correspond to what should be observed on anatomical images in an ideal scenario that assumes perfectly accurate B_1^+ maps, no patient motion and no other phenomena that affect the image homogeneity such as coil sensitivity and T_2^* effects. Lower homogeneity improvements are therefore expected for actual anatomical imaging experiments, because of the aforementioned effects.

4.3.2 Improved signal homogeneity along the spine

Figure 4.5 and Figure 4.6 compare sagittal slices acquired with CP mode and B_1^+ shimming in the center of the spine of the 2 subjects. Normalized UNI (a, b) and INV2 GRE (c, d) images are shown and the values in the segmented spinal cord are colored for better visualization. For subject 1 and 2, the B_1^+ CV in the spinal cord were respectively reduced by 39.72% and 10.59% on the INV2 GRE image and by 22.15% and 6.17% on the MP2RAGE UNI image. The lower CV reduction on UNI images compared to INV2 images (notably for subject 1) tends to confirm that the

computation of UNI images partially gets rid of the B_1^+ inhomogeneities. However, they still seem to benefit from B_1^+ shimming. As UNI images are strongly T_1 weighted, these results suggest that B_1^+ shimming may be used to reduce B_1^+ biases for T_1 measurement in the spinal cord, even with a relatively unbiased sequence such as MP2RAGE.

The CV difference observed between the B_1^+ shimmed INV2 images (Figure 4.5 d and Figure 4.6 d) and the ideally expected shimmed B_1^+ distributions (Figure 4.3 b and Figure 4.4 b) suggests that B_1^+ inhomogeneities are not the only cause of intensity variations on structural MR images. Indeed, despite a homogenized transmit distribution, the image homogeneity seems to still suffer from other effects, possibly related to inhomogeneous receive sensitivity, proton density or T_2^* relaxation.

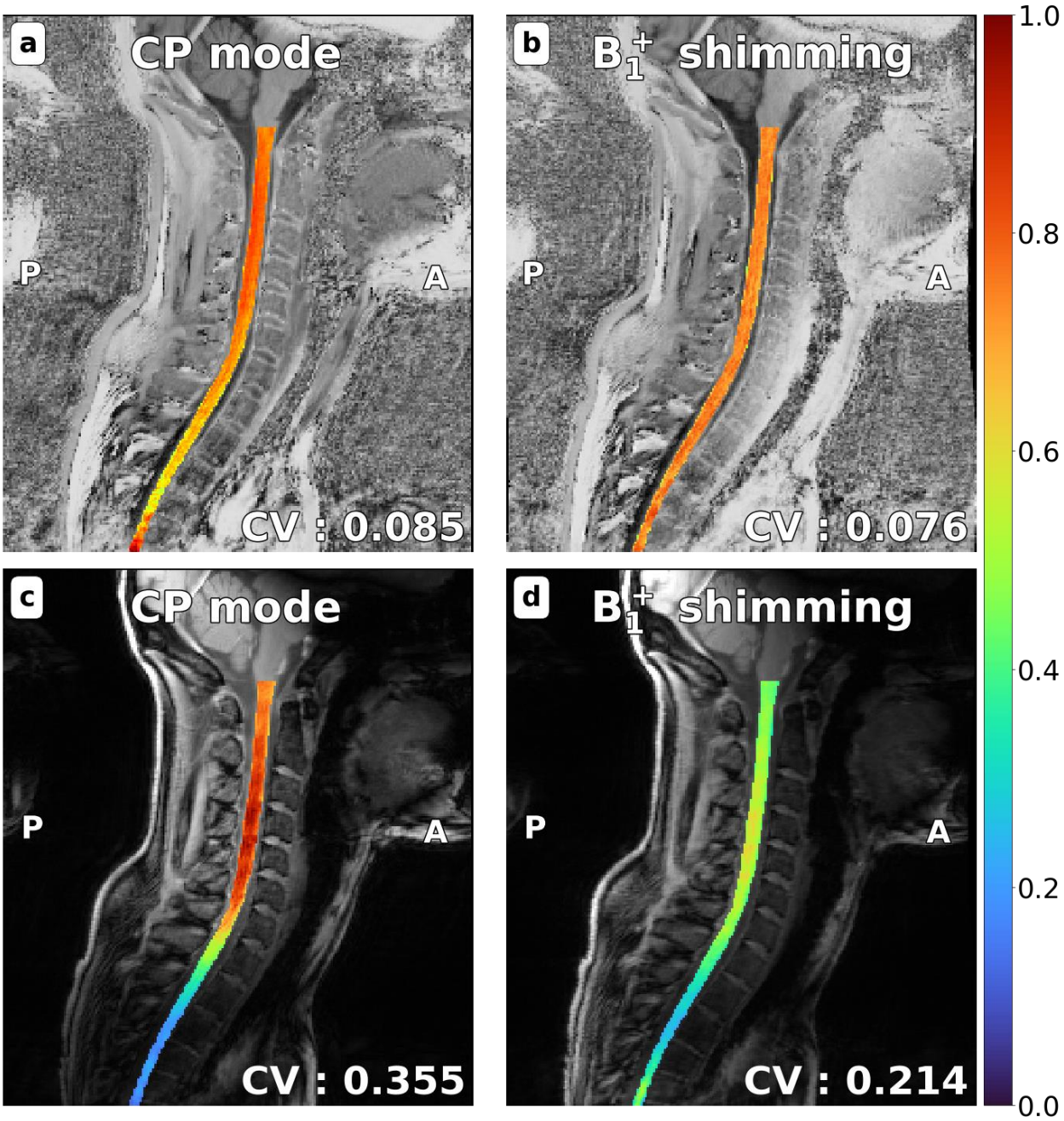

Figure 4.5 Normalized UNI and GRE images intensity in the spinal cord (subject 1). Spinal cords were manually segmented on shimmed and unshimmed images. After shimming the coefficient of variation in the spinal cord is reduced by 10.59% on UNI images (a, b) and 39.72% on INV2 GRE images (c, d).

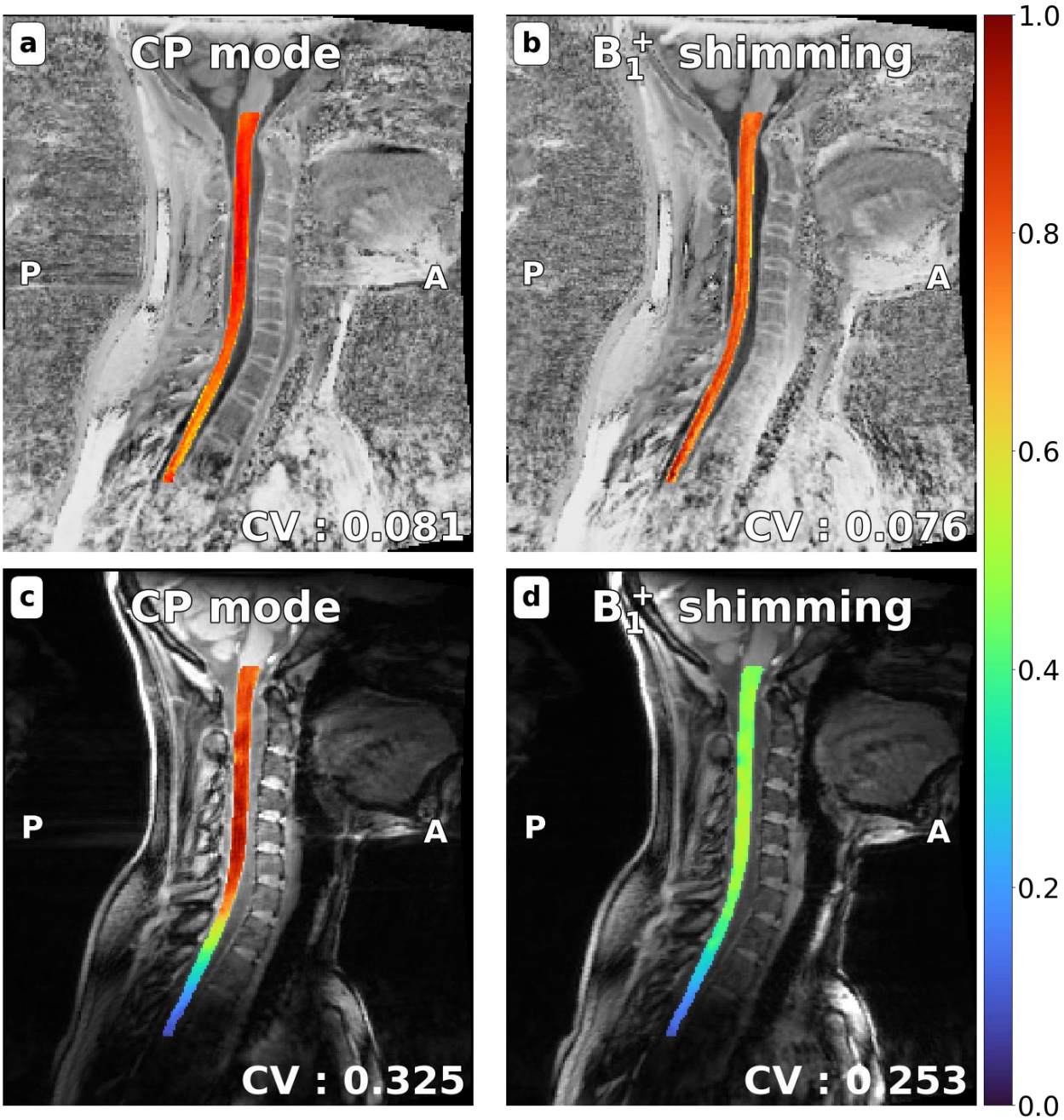

Figure 4.6 Normalized UNI and GRE images intensity in the spinal cord (subject 2). Spinal cords were manually segmented on shimmed and unshimmed images. After shimming the coefficient of variation in the spinal cord is reduced by 6.17% on UNI images (a, b) and 22.15% on INV2 GRE images (c, d).

In the case of subject 2, the automatic segmentation used as a shimming ROI (Figure 4.4) does not include many voxels of the thoracic part of the spinal cord. This may explain why less signal is recovered in the thoracic spinal cord on INV2 GRE images after shimming than for subject 1 (Figure 4.5 and Figure 4.6).

Figure 4.7 shows the CP mode and B_1^+ shimming mean intensity profiles along the segmented spinal cord on UNI images for subject 1. Mean intensity is computed for each axial slice in the manually segmented ROI shown on Figure 4.5. One can observe that the shimmed profile is much more homogeneous than the CP mode, especially in the thoracic region. The CV of these line profiles are respectively 0.77 and 0.22 for CP mode and B_1^+ shimming, indicating a 71.4% decrease.

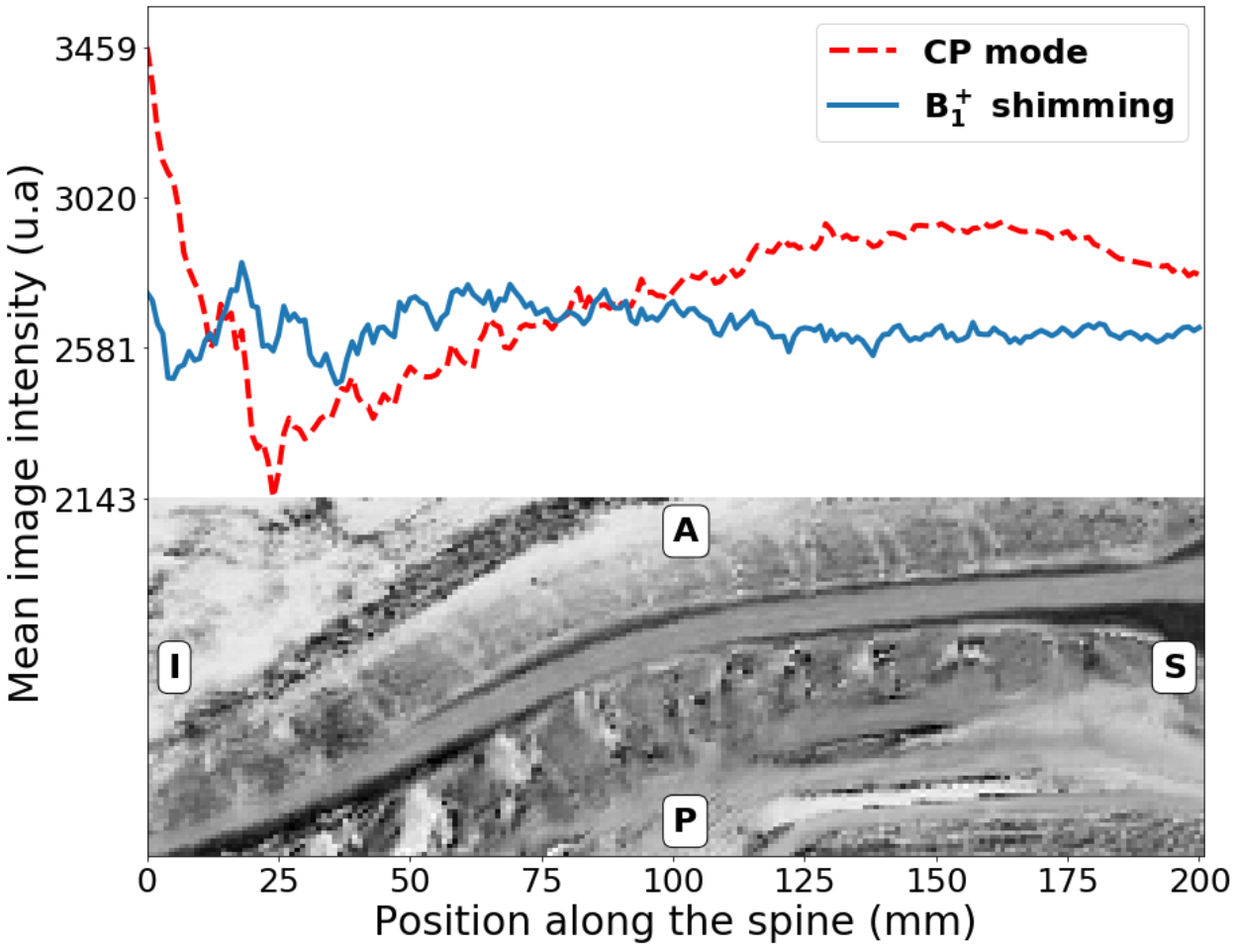

Figure 4.7 Mean UNI intensity profile across slices on UNI images (subject 1). Mean values are computed in the manually segmented spinal-cord.

For subject 2, T_1 maps were directly acquired along the MP2RAGE sequence before and after shimming and are shown in Figure 4.8. T_1 values were computed using Siemens' proprietary *MapIt* function. The spinal cord being mainly composed of white matter ($T_{1_{WM}}$ = 1126±97ms at 7T) and grey matter ($T_{1_{GM}}$ = 1939±149ms at 7T) [86], the mean T_1 value measured after shimming (1543ms) appear to be coherent with literature. After shimming the T_1 values are 12.23% more homogeneous along the segmented spinal cord. This suggests that B_1^+ could reduce the B_1^+ bias on T_1 measurements in the spinal cord.

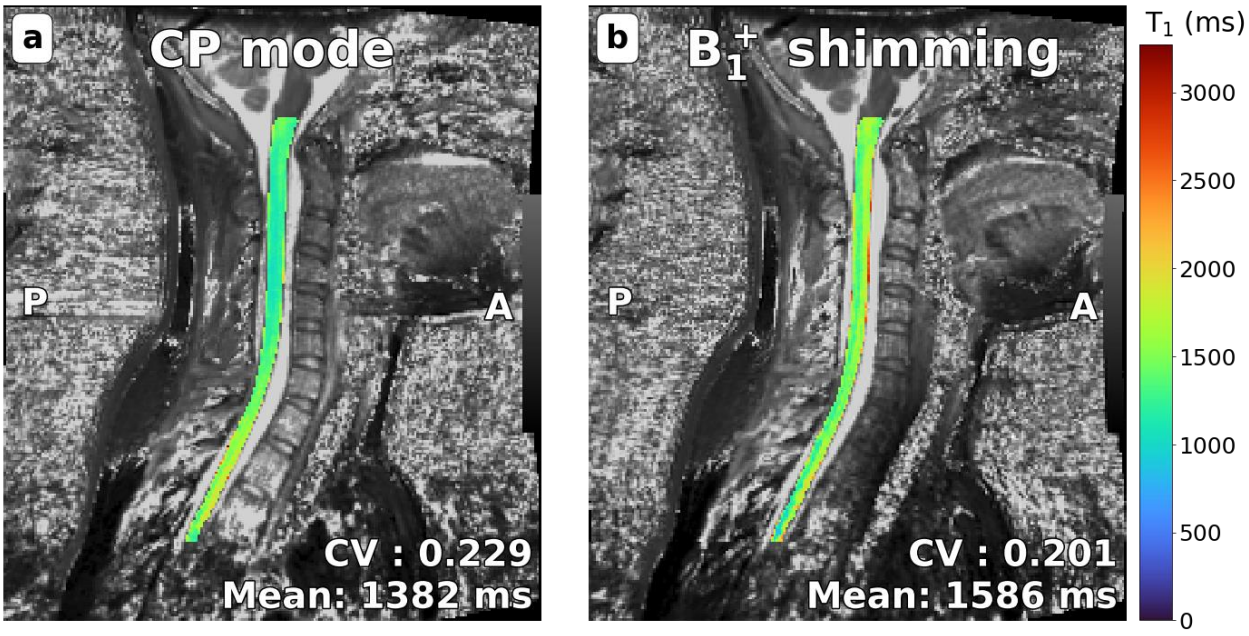

Figure 4.8 T_1 measurement in the segmented spinal cord before and after B_1^+ shimming. Spinal cords were manually segmented on shimmed and unshimmed images and a co-registration was performed.

CHAPTER 5 GENERAL DISCUSSION

5.1 B_1^+ shimming with Shimming-Toolbox

All proposed shim weights optimization algorithms resulted in the expected improved homogenization or increased B_1^+ efficiency when combined with the measured B_1^+ maps. However, as the shim weights optimization is generally a non-convex optimization problem, and despite the efforts that have been made to avoid this scenario, such as performing several initial phase-only optimizations with random starting values, the possibility of obtaining a sub-optimal set of shim weights still exists. But for all simulated, phantom, and in-vivo data on which the different optimization algorithms have been tested, sub-optimal solutions only seem to occur on rare occasions, and still always result in a significant improvement of the B_1^+ homogeneity or efficiency. Moreover, as non-convex optimization is an active area of research motivated by the fast widening of deep learning technologies [78], the development of more efficient state of the art optimization methods could benefit our B_1^+ shimming algorithms in the future, by improving their robustness against sub-optimal convergence.

Currently, the implemented B_1^+ shimming solution is only compatible with DICOM files acquired using the *Siemens* standard TurboFLASH B_1^+ sequence, limiting its use to a very limited number of research groups with access to that sequence. *Shimming-Toolbox* would thus highly benefit from compatibility with other manufacturers' native B_1^+ mapping sequences.

Moreover, the accuracy of the TurboFLASH B_1^+ sequence has not been evaluated in this study due to the lack of a gold standard method for individual B_1^+ mapping available on the scanner. A more accurate mapping could therefore further increase the shimming benefits by providing a better matching of the optimized B_1^+ distribution and the actual in-vivo distribution.

Another major limitation of this B_1^+ shimming implementation is the time currently required to manually input the optimized shim weights on the scanner. For an 8 Tx channel coil as the one used for our in-vivo tests, this input step requires approximately 1 minute. But as the number of Tx channels increases, the required time to input the shim weights will itself increase proportionally.

5.2 In-vivo B_1^+ shimming in the spinal cord

The preliminary in-vivo tests of *Shimming-Toolbox* for B_1^+ shimming in the spinal cord at 7T resulted in an improvement of the signal homogeneity along the spinal cord in different subjects, simultaneously demonstrating that the toolbox works as expected, and that spinal-cord imaging applications might benefit from patient-specific B_1^+ shimming.

A caveat of the B_1^+ mapping TurboFLASH sequence is that, when used with our custom spine coil, it results in an important masking in the regions with low SNR as observed in Figure 4.3 and Figure 4.4 in the anterior part of the neck, around the subject's mouth and in the thoracic region. This masking seems to be applied during the reconstruction of the B_1^+ maps but no mean of reducing it was found. This masking affects the B_1^+ shimming efficiency because shimming over the masked-out regions is impossible, as the individual B_1^+ distributions in these voxels are unknown. However, as we managed to get few to no masking in the spinal cord for some of the scanned subjects presented in this work, we decided that this B_1^+ mapping sequence would be sufficient for the scope of our study that only aimed at providing preliminary evaluations of the benefits of B_1^+ shimming in the spinal cord.

B_1^+ shimming along the spinal cord allows us to take better advantage of our coil geometry, as it recovers signal in the thoracic region and improves the image homogeneity in the occipital lobe to the mid-thoracic spinal cord. It may also improve T1 mapping applications by reducing the B_1^+ biases that may affect such measurements [87].

In this work, B_1^+ shimming results are compared with images obtained using a CP mode optimized for imaging the cervical region. Using a CP mode optimized over the whole spinal cord could also improve the signal homogeneity along the spinal cord without requiring any additional scanning time, but it would not be as efficient as a patient-specific B_1^+ shimming approach, one reason being that patient-specific optimized shim weights account for the important anatomical variability of the spine region across subjects.

CHAPTER 6 CONCLUSION AND RECOMMENDATIONS

This work resulted in the successful implementation of an open source B_1^+ shimming toolbox, allowing any researcher operating on a *Siemens* 7T MRI scanner to perform the most common static B_1^+ shimming experiments with a few minutes of additional scan-time. The user interface makes the toolbox particularly user friendly and easy to operate. The handling of NIfTI files makes *Shimming-Toolbox* compatible with many popular automated segmentation tools, allowing for localized and efficient homogenization of specific anatomical regions.

However, as previously discussed, *Shimming-Toolbox's* B_1^+ shimming implementation remains limited to *Siemens* sites. The most straightforward continuity of this work would thus be to implement compatibility with other manufacturers in order to reach a wider range of potential users.

This software implementation was used to demonstrate the potential clinical benefits of B_1^+ shimming for UHF spinal cord imaging with a custom coil, with an improved signal homogeneity, recovered signal in the lower spine, and a more accurate segmentation. These promising in-vivo results may draw the attention of other research groups and motivate them to use *Shimming-Toolbox* according to their needs. The feedback received from these potential users would moreover be the best way to ensure that our toolbox efficiently covers the needs of the MRI community in terms of shimming.

For future investigations related to B_1^+ shimming in the spinal cord, it would be of interest to evaluate the benefits of slice-by-slice B_1^+ shimming [16] for spinal cord imaging, taking advantage of the small cross section of the spinal cord on axial slices to further homogenize the B_1^+ efficiency. Indeed, by performing a shim weights optimization over a very small number of voxels on a slice-by-slice basis, one can expect to obtain a very homogeneous B_1^+ distribution. The main challenge of such a study would likely be the implementation of an imaging sequence capable of reading in real time a file containing an optimized set of complex shim weights for each imaged slice. Such a sequence could then be made available to the community and the slice-by-slice optimization be implemented as a *Shimming-Toolbox* feature.

Another promising B_1^+ shimming method whose benefits have yet to be explored for spinal cord imaging is the design of Universal Pulses (UP) [58]. However, while UP proved particularly good at homogenizing B_1^+ fields in the brain, their efficiency might be affected by the important inter-subject anatomical variability of the spine region. But one may still consider developing different pulses for various anatomies (e.g., one UP for large subject and one other for small subjects).

REFERENCES

[1] I. I. Rabi, J. R. Zacharias, S. Millman, and P. Kusch, "A New Method of Measuring Nuclear Magnetic Moment," *Phys. Rev.*, vol. 53, no. 4, pp. 318–318, Feb. 1938.

[2] F. Bloch, W. W. Hansen, and M. Packard, "The nuclear induction experiment," *Physical review*, vol. 70, no. 7–8, pp. 474–485, 1946.

[3] E. M. Purcell, H. C. Torrey, and R. V. Pound, "Resonance Absorption by Nuclear Magnetic Moments in a Solid," *Phys. Rev.*, vol. 69, no. 1–2, pp. 37–38, Jan. 1946.

[4] R. Damadian, "Tumor detection by nuclear magnetic resonance," *Science*, vol. 171, no. 3976, pp. 1151–1153, Mar. 1971.

[5] R. Damadian, M. Goldsmith, and L. Minkoff, "NMR IN CANCER: XVI. FONAR IMAGE OF THE UVE HUMAN BODY," 1977.

[6] P. C. Lauterbur, "Image Formation by Induced Local Interactions: Examples Employing Nuclear Magnetic Resonance," *Nature*, vol. 242, no. 5394. pp. 190–191, 1973.

[7] P. Mansfield and A. A. Maudsley, "Medical imaging by NMR," *Br. J. Radiol.*, vol. 50, no. 591, pp. 188–194, Mar. 1977.

[8] A. Sadeghi-Tarakameh *et al.*, "In vivo human head MRI at 10.5T: A radiofrequency safety study and preliminary imaging results," *Magn. Reson. Med.*, vol. 84, no. 1, pp. 484–496, Jul. 2020.

[9] E. E. Sigmund *et al.*, "High-resolution human cervical spinal cord imaging at 7 T," *NMR Biomed.*, vol. 25, no. 7, pp. 891–899, Jul. 2012.

[10] A. S. Nielsen, R. P. Kinkel, E. Tinelli, T. Benner, J. Cohen-Adad, and C. Mainero, "Focal cortical lesion detection in multiple sclerosis: 3 Tesla DIR versus 7 Tesla FLASH-T2," *J. Magn. Reson. Imaging*, vol. 35, no. 3, pp. 537–542, Mar. 2012.

[11] S. Trattnig *et al.*, "Key clinical benefits of neuroimaging at 7T," *Neuroimage*, vol. 168, pp. 477–489, Mar. 2018.

[12] J. Galley, R. Sutter, C. Germann, F. Wanivenhaus, and D. Nanz, "High-resolution in vivo MR imaging of intraspinal cervical nerve rootlets at 3 and 7 Tesla," *Eur. Radiol.*, vol. 31, no. 7, pp. 4625–4633, Jul. 2021.

[13] T. S. Ibrahim, R. Lee, A. M. Abduljalil, B. A. Baertlein, and P.-M. L. Robitaille, "Dielectric resonances and B1 field inhomogeneity in UHF MRI: computational analysis and experimental findings," 2001. [Online]. Available: http://dx.doi.org/10.1016/S0730-725X(01)00300-9. [Accessed: 10-Aug-2020].

[14] C. M. Collins, W. Liu, W. Schreiber, Q. X. Yang, and M. B. Smith, "Central brightening due to constructive interference with, without, and despite dielectric resonance," *J. Magn. Reson. Imaging*, vol. 21, no. 2, pp. 192–196, Feb. 2005.

[15] G. J. Metzger, C. Snyder, C. Akgun, T. Vaughan, K. Ugurbil, and P.-F. Van de Moortele, "Local B1+ shimming for prostate imaging with transceiver arrays at 7T based on subject-dependent transmit phase measurements," *Magn. Reson. Med.*, vol. 59, no. 2, pp. 396–409, Feb. 2008.

[16] A. T. Curtis, K. M. Gilbert, L. M. Klassen, J. S. Gati, and R. S. Menon, “Slice-by-slice B1+ shimming at 7 T,” *Magn. Reson. Med.*, vol. 68, no. 4, pp. 1109–1116, Oct. 2012.

[17] A. Paez, C. Gu, and Z. Cao, “Robust RF shimming and small-tip-angle multispoke pulse design with finite-difference regularization,” *Magn. Reson. Med.*, May 2021.

[18] A. D’astous *et al.*, “Shimming-Toolbox: An open-source software package for performing realtime B0 shimming experiments,” in *Proceedings of the 30th Annual Meeting of ISMRM*, 2021.

[19] O. Kraff *et al.*, “An eight-channel phased array RF coil for spine MR imaging at 7 T,” *Invest. Radiol.*, vol. 44, no. 11, pp. 734–740, Nov. 2009.

[20] B. Wu *et al.*, “7T human spine imaging arrays with adjustable inductive decoupling,” *IEEE Trans. Biomed. Eng.*, vol. 57, no. 2, pp. 397–403, Feb. 2010.

[21] W. Zhao *et al.*, “Nineteen-channel receive array and four-channel transmit array coil for cervical spinal cord imaging at 7T,” *Magn. Reson. Med.*, vol. 72, no. 1, pp. 291–300, Jul. 2014.

[22] S. H. G. Rietsch *et al.*, “Development and evaluation of a 16-channel receive-only RF coil to improve 7T ultra-high field body MRI with focus on the spine,” *Magn. Reson. Med.*, vol. 82, no. 2, pp. 796–810, Aug. 2019.

[23] N. Lopez Rios *et al.*, “Integrated AC/DC coil and dipole Tx array for 7T MRI of the spinal cord,” in *27th Annual Meeting of ISMRM, Montreal, Canada*, 2019, p. 220.

[24] M. W. May *et al.*, “A Patient-Friendly 16ch Tx / 64ch Rx Array for Combined Head and Neck Imaging at 7 Tesla,” in *Proceedings of the 21st Annual Meeting of ISMRM*, p. 181.

[25] R. W. Brown, Y.-C. N. Cheng, E. Mark Haacke, M. R. Thompson, and R. Venkatesan, *Magnetic Resonance Imaging: Physical Principles and Sequence Design*. John Wiley & Sons, 2014.

[26] A. Deshmane, V. Gulani, M. A. Griswold, and N. Seiberlich, “Parallel MR imaging,” *J. Magn. Reson. Imaging*, vol. 36, no. 1, pp. 55–72, Jul. 2012.

[27] A. Nowogrodzki, “The world’s strongest MRI machines are pushing human imaging to new limits,” *Nature*, vol. 563, no. 7729, pp. 24–26, Nov. 2018.

[28] M. Goldman, “Formal theory of spin--lattice relaxation,” *J. Magn. Reson.*, vol. 149, no. 2, pp. 160–187, Apr. 2001.

[29] D. I. Hoult, “The principle of reciprocity in signal strength calculations?A mathematical guide,” *Concepts Magn. Reson.*, vol. 12, no. 4, pp. 173–187, 2000.

[30] T. S. Ibrahim, Y.-K. Hue, and L. Tang, “Understanding and manipulating the RF fields at high field MRI,” *NMR Biomed.*, vol. 22, no. 9, pp. 927–936, Nov. 2009.

[31] Q. X. Yang *et al.*, “Analysis of wave behavior in lossy dielectric samples at high field,” *Magn. Reson. Med.*, vol. 47, no. 5, pp. 982–989, May 2002.

[32] C. Gabriel, “Compilation of the Dielectric Properties of Body Tissues at RF and Microwave Frequencies,” Feb. 1996.

[33] Y. Rahmat-Samii and J. Kim, “Implanted Antennas in Medical Wireless Communications,” *Synthesis Lectures on Antennas*, vol. 1, no. 1, pp. 1–82, Jan. 2006.

[34] F. Schick, “Whole-body MRI at high field: technical limits and clinical potential,” *Eur. Radiol.*, vol. 15, no. 5, pp. 946–959, May 2005.

[35] P. Röschmann, “Radiofrequency penetration and absorption in the human body: limitations to high-field whole-body nuclear magnetic resonance imaging,” *Med. Phys.*, vol. 14, no. 6, pp. 922–931, Nov. 1987.

[36] E. R. McVeigh, M. J. Bronskill, and R. M. Henkelman, “Phase and sensitivity of receiver coils in magnetic resonance imaging,” *Med. Phys.*, vol. 13, no. 6, pp. 806–814, Nov. 1986.

[37] M. I. Vargas *et al.*, “Clinical Neuroimaging Using 7 T MRI: Challenges and Prospects,” *J. Neuroimaging*, vol. 28, no. 1, pp. 5–13, Jan. 2018.

[38] B. Gruber, M. Froeling, T. Leiner, and D. W. J. Klomp, “RF coils: A practical guide for nonphysicists,” *J. Magn. Reson. Imaging*, Jun. 2018.

[39] A. A. Hurshkainen *et al.*, “A parametric study of radiative dipole body array coil for 7 Tesla MRI,” *Photonics Nanostruct. Fundam. Appl.*, vol. 39, p. 100764, May 2020.

[40] T. Santini, S. Wood, N. Krishnamurthy, T. Martins, H. J. Aizenstein, and T. S. Ibrahim, “Improved 7 Tesla transmit field homogeneity with reduced electromagnetic power deposition using coupled Tic Tac Toe antennas,” *Sci. Rep.*, vol. 11, no. 1, p. 3370, Feb. 2021.

[41] I. A. Elabyad, M. Terekhov, M. Bille, and L. M. Schreiber, “Design and Implementation of Two 16-Element Antisymmetric Transceiver Coil Arrays for Parallel Transmission Human Cardiac MRI at 7 T,” *IEEE Trans. Microw. Theory Tech.*, vol. 69, no. 7, pp. 3540–3557, Jul. 2021.

[42] W. M. Brink, J. S. van den Brink, and A. G. Webb, “The effect of high-permittivity pads on specific absorption rate in radiofrequency-shimmed dual-transmit cardiovascular magnetic resonance at 3T,” *J. Cardiovasc. Magn. Reson.*, vol. 17, p. 82, Sep. 2015.

[43] W. M. Brink, M. J. Versluis, J. M. Peeters, P. Börnert, and A. G. Webb, “Passive radiofrequency shimming in the thighs at 3 Tesla using high permittivity materials and body coil receive uniformity correction,” *Magn. Reson. Med.*, vol. 76, no. 6, pp. 1951–1956, Dec. 2016.

[44] Y. Hwang, H. Noh, M. Park, J. Lee, and N. Park, “B1+ Homogenization in 7T MRI Using Mode-shaping with High Permittivity Materials,” *arXiv [physics.med-ph]*, 13-Nov-2019.

[45] S. Ullah and H. Yoo, “Performance Enhancement of an MTL Coil Loaded With High-Permittivity Dielectric Liner for 7 T Brain MRI,” *IEEE Access*, vol. 9, pp. 144417–144425, 2021.

[46] M. S. Cohen, R. M. DuBois, and M. M. Zeineh, “Rapid and effective correction of RF inhomogeneity for high field magnetic resonance imaging,” *Hum. Brain Mapp.*, vol. 10, no. 4, pp. 204–211, Aug. 2000.

[47] J. Wang, M. Qiu, Q. X. Yang, M. B. Smith, and R. T. Constable, “Measurement and correction of transmitter and receiver induced nonuniformities in vivo,” *Magn. Reson. Med.*, vol. 53, no. 2, pp. 408–417, Feb. 2005.

[48] S. Saekho, C.-Y. Yip, D. C. Noll, F. E. Boada, and V. A. Stenger, "Fast-kz three-dimensional tailored radiofrequency pulse for reduced B1 inhomogeneity," *Magn. Reson. Med.*, vol. 55, no. 4, pp. 719–724, Apr. 2006.

[49] N. Boulant, D. Le Bihan, and A. Amadon, "Strongly modulating pulses for counteracting RF inhomogeneity at high fields," *Magn. Reson. Med.*, vol. 60, no. 3, pp. 701–708, Sep. 2008.

[50] N. Boulant, J.-F. Mangin, and A. Amadon, "Counteracting radio frequency inhomogeneity in the human brain at 7 Tesla using strongly modulating pulses," *Magn. Reson. Med.*, vol. 61, no. 5, pp. 1165–1172, May 2009.

[51] G. H. Glover *et al.*, "Comparison of linear and circular polarization for magnetic resonance imaging," *J. Magn. Reson.*, vol. 64, no. 2, pp. 255–270, Sep. 1985.

[52] C. M. Deniz, "Parallel Transmission for Ultrahigh Field MRI," *Top. Magn. Reson. Imaging*, vol. 28, no. 3, pp. 159–171, Jun. 2019.

[53] B. Van Den Bergen, C. A. T. Van den Berg, L. W. Bartels, and J. J. W. Lagendijk, "7 T body MRI: B1 shimming with simultaneous SAR reduction," *Physics in Medicine & Biology*, vol. 52, no. 17, p. 5429, 2007.

[54] C. M. Deniz, R. Brown, R. Lattanzi, L. Alon, D. K. Sodickson, and Y. Zhu, "Maximum efficiency radiofrequency shimming: Theory and initial application for hip imaging at 7 tesla," *Magn. Reson. Med.*, vol. 69, no. 5, pp. 1379–1388, May 2013.

[55] W. Mao, M. B. Smith, and C. M. Collins, "Exploring the limits of RF shimming for high-field MRI of the human head," *Magn. Reson. Med.*, vol. 56, no. 4, pp. 918–922, Oct. 2006.

[56] U. Katscher, P. Börnert, C. Leussler, and J. S. van den Brink, "Transmit SENSE," *Magn. Reson. Med.*, vol. 49, no. 1, pp. 144–150, Jan. 2003.

[57] M. A. Cloos *et al.*, "kT-points: short three-dimensional tailored RF pulses for flip-angle homogenization over an extended volume," *Magn. Reson. Med.*, vol. 67, no. 1, pp. 72–80, 2012.

[58] V. Gras, A. Vignaud, and A. Amadon, "Universal pulses: a new concept for calibration-free parallel transmission," *Magnetic resonance*, 2017.

[59] R. Tomi-Tricot *et al.*, "SmartPulse, a machine learning approach for calibration-free dynamic RF shimming: Preliminary study in a clinical environment," *Magn. Reson. Med.*, vol. 82, no. 6, pp. 2016–2031, Dec. 2019.

[60] C. C. Johnson and A. W. Guy, "Nonionizing electromagnetic wave effects in biological materials and systems," *Proc. IEEE*, vol. 60, no. 6, pp. 692–718, Jun. 1972.

[61] P. A. Bottomley and E. R. Andrew, "RF magnetic field penetration, phase shift and power dissipation in biological tissue: implications for NMR imaging," *Phys. Med. Biol.*, vol. 23, no. 4, pp. 630–643, Jul. 1978.

[62] E. M. Shapiro, A. Borthakur, M. J. Shapiro, R. Reddy, and J. S. Leigh, "Fast MRI of RF heating via phase difference mapping," *Magn. Reson. Med.*, vol. 47, no. 3, pp. 492–498, Mar. 2002.

[63] H. Cline, R. Mallozzi, Z. Li, G. McKinnon, and W. Barber, "Radiofrequency power deposition utilizing thermal imaging," *Magn. Reson. Med.*, vol. 51, no. 6, pp. 1129–1137, Jun. 2004.

[64] T. Voigt, H. Homann, U. Katscher, and O. Doessel, “Patient-individual local SAR determination: in vivo measurements and numerical validation,” *Magn. Reson. Med.*, vol. 68, no. 4, pp. 1117–1126, Oct. 2012.

[65] H. Jeong, M. C. Restivo, P. Jezzard, and A. T. Hess, “Assessment of radio-frequency heating of a parallel transmit coil in a phantom using multi-echo proton resonance frequency shift thermometry,” *Magn. Reson. Imaging*, vol. 77, pp. 57–68, Apr. 2021.

[66] B. Guérin, M. Gebhardt, S. Cauley, E. Adalsteinsson, and L. L. Wald, “Local specific absorption rate (SAR), global SAR, transmitter power, and excitation accuracy trade-offs in low flip-angle parallel transmit pulse design,” *Magnetic Resonance in Medicine*, vol. 71, no. 4. pp. 1446–1457, 2014.

[67] P. Bernardi, M. Cavagnaro, S. Pisa, and E. Piuzzi, “Specific absorption rate and temperature elevation in a subject exposed in the far-field of radio-frequency sources operating in the 10-900-MHz range,” *IEEE Trans. Biomed. Eng.*, vol. 50, no. 3, pp. 295–304, Mar. 2003.

[68] I. E. Commission and Others, “Medical electrical equipment-Part 2-33: Particular requirements for the basic safety and essential performance of magnetic resonance equipment for medical diagnosis,” *IEC 60601-2-33 Ed. 3. 0*, 2010.

[69] S. Reiss, A. Bitzer, and M. Bock, “An optical setup for electric field measurements in MRI with high spatial resolution,” *Phys. Med. Biol.*, vol. 60, no. 11, pp. 4355–4370, Jun. 2015.

[70] T. M. Fiedler, M. E. Ladd, and A. K. Bitz, “SAR Simulations & Safety,” *Neuroimage*, vol. 168, pp. 33–58, Mar. 2018.

[71] I. Graesslin *et al.*, “A specific absorption rate prediction concept for parallel transmission MR,” *Magn. Reson. Med.*, vol. 68, no. 5, pp. 1664–1674, Nov. 2012.

[72] G. Eichfelder and M. Gebhardt, “Local specific absorption rate control for parallel transmission by virtual observation points,” *Magn. Reson. Med.*, vol. 66, no. 5, pp. 1468–1476, Nov. 2011.

[73] S. Orzada, T. M. Fiedler, A. K. Bitz, M. E. Ladd, and H. H. Quick, “Local SAR compression with overestimation control to reduce maximum relative SAR overestimation and improve multi-channel RF array performance,” *MAGMA*, Sep. 2020.

[74] S. Akoka, F. Franconi, F. Seguin, and A. Le Pape, “Radiofrequency map of an NMR coil by imaging,” *Magn. Reson. Imaging*, vol. 11, no. 3, pp. 437–441, 1993.

[75] V. L. Yarnykh, “Actual flip-angle imaging in the pulsed steady state: a method for rapid three-dimensional mapping of the transmitted radiofrequency field,” *Magn. Reson. Med.*, vol. 57, no. 1, pp. 192–200, Jan. 2007.

[76] L. I. Sacolick, F. Wiesinger, I. Hancu, and M. W. Vogel, “B1 mapping by Bloch-Siegert shift,” *Magnetic Resonance in Medicine*, vol. 63, no. 5. pp. 1315–1322, 2010.

[77] S. Chung, D. Kim, E. Breton, and L. Axel, “Rapid B1+ mapping using a preconditioning RF pulse with TurboFLASH readout,” *Magn. Reson. Med.*, vol. 64, no. 2, pp. 439–446, Aug. 2010.

[78] M. Danilova *et al.*, “Recent Theoretical Advances in Non-Convex Optimization,” *arXiv [math.OC]*, 11-Dec-2020.

[79] N. I. Avdievich *et al.*, “Evaluation of transmit efficiency and SAR for a tight fit transceiver human head phased array at 9.4 T,” *NMR Biomed.*, vol. 30, no. 2, Feb. 2017.

[80] D. Kraft and Others, “A software package for sequential quadratic programming,” 1988.

[81] V. Pfaffenrot *et al.*, “An 8/15-channel Tx/Rx head neck RF coil combination with region-specific B1 + shimming for whole-brain MRI focused on the cerebellum at 7T,” *Magn. Reson. Med.*, vol. 80, no. 3, pp. 1252–1265, Sep. 2018.

[82] D. Rivera *et al.*, “Inherently decoupled 1 H antennas and 31 P loops for metabolic imaging of liver metastasis at 7 T,” *NMR Biomed.*, vol. 33, no. 4, p. e4221, Apr. 2020.

[83] J. P. Marques, T. Kober, G. Krueger, W. van der Zwaag, P.-F. Van de Moortele, and R. Gruetter, “MP2RAGE, a self bias-field corrected sequence for improved segmentation and T1-mapping at high field,” *Neuroimage*, vol. 49, no. 2, pp. 1271–1281, Jan. 2010.

[84] U.-S. Choi, H. Kawaguchi, Y. Matsuoka, T. Kober, and I. Kida, “Brain tissue segmentation based on MP2RAGE multi-contrast images in 7 T MRI,” *PLoS One*, vol. 14, no. 2, p. e0210803, Feb. 2019.

[85] B. De Leener *et al.*, “SCT: Spinal Cord Toolbox, an open-source software for processing spinal cord MRI data,” *Neuroimage*, vol. 145, no. Pt A, pp. 24–43, Jan. 2017.

[86] P. J. Wright *et al.*, “Water proton T1 measurements in brain tissue at 7, 3, and 1.5 T using IR-EPI, IR-TSE, and MPRAGE: results and optimization,” *MAGMA*, vol. 21, no. 1–2, pp. 121–130, Mar. 2008.

[87] N. Weiskopf, A. Lutti, G. Helms, M. Novak, J. Ashburner, and C. Hutton, “Unified segmentation based correction of R1 brain maps for RF transmit field inhomogeneities (UNICORT),” *Neuroimage*, vol. 54, no. 3, pp. 2116–2124, Feb. 2011.